Transcriptomic and spatial GABAergic neuron subtypes in zona incerta mediate distinct innate behaviors

Mengyue Zhu[1,2 #], Jieqiao Peng[1,2 #], Mi Wang[1,2 #], Shan Lin[1,2 #], Huiying Zhang[3#], Yu Zhou[1,2], Xinyue Dai[1,2], Huiying Zhao[1,2], Yan-qin Yu[1,2], Li Shen[3], Xiao-Ming Li[1,2,4 *], Jiadong Chen[1,2,5 *]

[1] Department of Neurobiology, Departments of Neurosurgery and Neurology of the Second Affiliated Hospital, Zhejiang University School of Medicine, Hangzhou 310058, China

[2] Nanhu Brain-computer Interface Institute, NHC and CAMS Key Laboratory of Medical Neurobiology, MOE Frontier Science Center for Brain Research and Brain-machine Integration, School of Brain Science and Brain Medicine, Zhejiang University, Hangzhou 310058, China

[3] The MOE Key Laboratory of Biosystems Homeostasis & Protection and Zhejiang Provincial Key Laboratory for Cancer Molecular Cell Biology, Life Sciences Institute, Zhejiang University, Hangzhou 310058, China

[4] Center for Brain Science and Brain-Inspired Intelligence, Research Units for Emotion and Emotion Disorders, Chinese Academy of Medical Sciences/ Guangdong–Hong Kong–Macao Greater Bay Area Center for Brain Science and Brain-Inspired Intelligence, Guangzhou 311305, China

[5] Lead Contact.

[#] These authors contributed equally to this work.

*Corresponding Authors: Xiao-Ming Li, Jiadong Chen

Email: lixm@zju.edu.cn; jardongchen@zju.edu.cn

Abstract

Understanding the anatomical connection and behaviors of transcriptomic neuron subtypes is critical to delineating cell type-specific functions in the brain. Here we integrated single-nucleus transcriptomic sequencing, *in vivo* circuit mapping, optogenetic and chemogenetic approaches to dissect the molecular identity and function of heterogeneous GABAergic neuron populations in the zona incerta (ZI) in mice, a region involved in modulating various behaviors. By microdissecting ZI for transcriptomic and spatial gene expression analyses, our results revealed two non-overlapping *Ecel1*- and *Pde11a*-expressing GABAergic neurons with dominant expression in the rostral and medial zona incerta (ZIr^{Ecel1} and ZIm^{Pde11a}), respectively. The GABAergic projection from ZIr^{Ecel1} to periaqueductal gray mediates self-grooming, while the GABAergic projection from ZIm^{Pde11a} to the oral part of pontine reticular formation promotes transition from sleep to wakefulness. Together, our results revealed the molecular markers, spatial organization and specific neuronal circuits of two discrete GABAergic projection neuron populations in segregated subregions of the ZI that mediate distinct innate behaviors, advancing our understanding of the functional organization of the brain.

Introduction

The molecular, morphological and anatomical features of neurons imply distinct neuronal subtypes, axonal projection pattern, and behavioral functions in the central nervous system[1, 2]. Recent advances in single-cell transcriptomics reveal cell type specific genes expression and molecular markers of transcriptomic cell subtypes[3-5]. Extensive efforts have been applied to classify neuron subtypes by morphological and electrophysiological characteristics[6-8], in conjunction with

single-cell transcriptomic analysis[9-13]. Spatial transcriptomic analysis discovered diverse cell subtypes and their anatomical organization across the whole brain[14-16]. In addition, the integrated retrograde or anterograde transsynaptic tracing with spatial transcriptomic analyses revealed the long-range synaptic connectivity of neuronal subtypes, connecting transcriptomic clusters with axonal projections at scale[4, 17-20]. However, the behavioral functions of different transcriptomic neuronal subtypes are yet to be determined in behaving animals. Therefore, investigating the anatomical connection and behavior of transcriptomic and spatial neuron subtypes is important to reveal the functional organization of the brain.

The GABAergic projection neurons establish long-range efferent projections and may promote efficient information transfer between distant brain networks compared with the well-studied cortical interneurons [21, 22]. Recent studies revealed the presence of long-range GABAergic projection neurons in various brain regions including the prefrontal cortex[23, 24], entorhinal cortex[25], hippocampus[25, 26], and also top-down afferents from the zona incerta (ZI)[27], basal ganglia[28], and septum[29], but their sparse distribution makes it difficult to identify the molecular markers for this heterogeneous population by conventional single-cell RNA sequencing approach[21, 22]. The zona incerta (ZI), located in the ventral thalamus, predominantly comprises GABAergic neurons that project to distant brain regions and mediate various behavioral functions[30, 31]. The heterogeneous neuron populations in the ZI can be divided into cytoarchitectonic subregions or sectors along the anteroposterior axis, which form extensive connections with multiple brain regions and may function as one of the integrative nodes in the brain[30-33]. Recent studies in rodents and non-human primates revealed various behavioral functions upon stimulating subregions of the ZI [34-42]. However, the lack of molecular markers makes it difficult to selectively target or to investigate the function of GABAergic projection neurons in different subregions of the ZI[21, 22].

In the present study, by microdissecting the ZI for single-nucleus transcriptomic sequencing, we investigated the molecular subtypes and spatial localization of GABAergic neuron populations in different subregions of the ZI.

Through constructing transgenic mice to label region-specific GABAergic neuron subtypes in ZI, integrated with *in vivo* circuit mapping, and optogenetic and chemogenetic manipulation, we revealed two discrete subpopulations of GABAergic projection neurons in segregated subregions of the ZI that exert distinct behavioral functions.

Results

Single-nuclei transcriptomic profiling revealed distinct cell clusters and region specific gene expression in the zona incerta

To analyze the molecular diversity of cell types in ZI, we micro-dissected the brain region according to the distribution of fluorescent reporter from postnatal day 40 (P40) Gad67-GFP transgenic mice in ZI and the anatomy from the reference mouse brain atlas of Allen Mouse Brain Common Coordinate Framework[33]. We dissociated the micro-dissected brain tissue into single nuclei suspension and analyzed the single-nuclei transcriptome of ZI in the adult mouse brain by 10x genomics. We harvested 15,375 single nuclei from two independent cohorts of 10x genomics single-nucleus RNA sequencing experiments and obtained similar cell clusters by reciprocal principle component analysis (RPCA) (Fig. 1a and Supplementary Fig. 1a-c). The cell clusters were displayed by uniform manifold approximation and projection (UMAP) and annotated with canonical cell type specific marker genes. We identified cell clusters including major cell types such as inhibitory neurons (*Rbfox3*, *Gad2*), excitatory neurons (*Rbfox3*, *Slc17a6*)[43-45], dopaminergic neurons (*Slc6a3*)[46, 47], microglia (*Cx3cr1*)[44, 48], astrocytes (*Aldh1a1*)[49], pericytes (*Pdgfrb*)[44], endothelial cells (*Cldn5*)[46, 47], oligodendrocyte precursor cells (OPCs, *Pdgfra*), differentiation-committed oligodendrocyte precursors (COPs, *Tns3*), oligodendrocytes (*Mog*) and mature oligodendrocytes (MOLs, *Apod*) [50](Fig. 1a and Supplementary Fig. 1d).

We further reclustered the neuronal populations and revealed 10 clusters of glutamatergic neurons (Glu_N1 – Glu_N10) and 12 clusters of GABAergic neurons

(GABA_N1 – GABA_N12) that showed distinct differentially expressed genes (DEGs) among neuron subtypes in ZI and neighboring brain regions (Fig. 1b, c). Based on *in situ* hybridization of gene expression in the adult mouse brain from Allen brain atlas (https://mouse.brain-map.org/)[51], we annotated the anatomical locations of neuronal clusters and identified marker genes for ZI and neighboring brain regions in the subcortical forebrain: ZI (*Pax6, Meis2*), thalamus (*Tcf7l2, Lef1*) located dorsal to ZI, subthalamus nucleus (*Ttc6, Pitx2*) located ventral to ZI, paraventricular nucleus (*Sim1*, *Ndst4*) located ventral-medial to ZI, and reticular nucleus (*Six3*, *Pvalb*) located dorsal-lateral to ZI (Supplementary Fig. 2a).

GABAergic neurons in ZI projected to multiple brain regions and were implicated in various behaviors, however, the molecular profiles of different GABAergic neuron subtypes remain incompletely understood. Our data revealed six GABAergic neuron clusters in ZI (GABA_N4 to GABA_N9, Fig. 1d, e; Supplementary Fig. 2b, c and Supplementary table 1). Differential gene expression analysis revealed marker genes for different GABAergic neuron clusters that exhibited different anatomical distribution pattern in ZI, as demonstrated by *in situ* hybridization of gene expression in the Allen Mouse Brain Atlas (https://mouse.brain-map.org/)[51]. The GABA_N9 neuron cluster highly expressed *Ecel1* (endothelin converting enzyme like 1). The GABA_N6, GABA_N7 and GABA_N8 neuron clusters shared differentially expressed genes and highly expressed *Cdh23* (cadherin related 23), *Pax6* (paired box 6) and *Pde11a* (phosphodiesterase 11A). The GABA_N4 neuron cluster highly expressed *Ptprk* (protein tyrosine phosphatase receptor type K) and *Nos1* (nitric oxide synthase 1) (Fig. 2a and Supplementary Fig. 2c). These results revealed distinct transcriptomic profiles and candidate marker genes for GABAergic neurons in the ZI by single-nucleus RNA sequencing analysis.

Candidate genes for GABAergic neuron subtypes in subregions of zona incerta

We validated the expression and spatial distribution of the above six GABAergic marker genes in different anatomical subregions of ZI along the

anteroposterior axis by fluorescence *in situ* hybridization (FISH). We found that *Ecel1* exhibited highest distribution in the rostral ZI (ZIr: 59.56 ± 0.93%; ZIm: 14.41 ± 1.33%; ZIc: 26.03 ± 1.76%) compared with other marker genes expression in the ZIr (*Cdh23*: 22.37 ± 1.40%; *Pax6*: 29.20 ± 1.83%; *Nos1*: 22.98 ± 1.68%; *Ptprk*: 25.59 ± 1.67%). The marker gene *Pde11a* exhibited highest and most selective distribution in the medial ZI (ZIm: 80.49 ± 1.57%; ZIr: 7.873 ± 0.55%; ZIc: 11.63 ± 2.04%) compared with other marker genes expression in the ZIm (*Cdh23*: 54.60 ± 0.89%; *Pax6*: 43.97 ± 1.79%; *Nos1*: 49.20 ± 5.38%). We found that 33.82 ± 6.63% of the total *Ptprk* positive cells in the ZI were distributed in the caudal ZI, but showed no significant difference between different subregions of ZI (ZIr: 25.59 ± 1.67%; ZIm: 40.59 ± 6.35%. Fig. 2b and Supplementary Fig. 2d).

We further demonstrated that the density of *Ecel1*$^+$ cells is relatively higher than *Pde11a*$^+$ or *Ptprk*$^+$ cells in the ZIr (*Ecel1*$^+$: 1848 ± 82.52 per mm^2; *Pde11a*$^+$: 134.8 ± 10.60 per mm^2; *Ptprk*$^+$: 444.9 ± 38.15 per mm^2), and showed few overlap with *Pde11a* and *Ptprk* (*Ecel1*$^+$: 410.0 ± 9.539 cells; *Ecel1*$^+$*Pde11a*$^+$: 9.33 ± 1.20 cells; *Ecel1*$^+$*Ptprk*$^+$: 43.33 ± 5.49 cells; *Pde11a*$^+$*Ptprk*$^+$: 4.33 ± 0.88 cells; *Ecel1*$^+$*Pde11a*$^+$*Ptprk*$^+$: 1.67 ± 0.33 cells). The *Pde11a*$^+$ cells show higher density in the ZIm (*Ecel1*$^+$: 85.77 ± 4.066 per mm^2; *Pde11a*$^+$: 268.2 ± 24.12 per mm^2; *Ptprk*$^+$: 136.2 ± 21.35 per mm^2) and also show very few overlap with *Ecel1* and *Ptprk* (*Pde11a*$^+$: 361.0 ± 23.81 cells; *Ecel1*$^+$*Pde11a*$^+$: 1.67 ± 0.67 cells; *Ecel1*$^+$*Ptprk*$^+$: 4.67 ± 0.88 cells; *Pde11a*$^+$*Ptprk*$^+$: 2.67 ± 0.33 cells; *Ecel1*$^+$*Pde11a*$^+$*Ptprk*$^+$: 0 ± 0 cells). In contrast, the density of *Ptprk*$^+$ cells showed little differences with *Ecel1*$^+$ or *Pde11a*$^+$ cells in the ZIc (*Ecel1*$^+$: 317.8 ± 34.96 per mm^2; *Pde11a*$^+$: 78.27 ± 14.38 per mm^2; *Ptprk*$^+$: 228.9 ± 42.81 per mm^2. Fig. 2c - e) and *Ptprk*$^+$ cells rarely overlap with *Ecel1*$^+$ or *Pde11a*$^+$ cells (*Ptprk*$^+$: 132.3 ± 16.13 cells; *Ecel1*$^+$*Pde11a*$^+$: 3.33 ± 0.33 cells; *Ecel1*$^+$*Ptprk*$^+$: 7.33 ± 0.88 cells; *Pde11a*$^+$*Ptprk*$^+$: 2.00 ± 0.58 cells; *Ecel1*$^+$*Pde11a*$^+$*Ptprk*$^+$: 2.33 ± 0.88 cells). These results demonstrated that the expression of *Ecel1* and *Pde11a* are non-overlapping across different subregions of the ZI along the anteroposterior axis (Fig. 2d, e). Together, these results revealed that *Ecel1*- and *Pde11a*-expressing GABAergic neurons are non-

overlapping and exhibit dominant expression in the rostral and medial ZI, respectively.

Ecel1-positive neurons in the rostral ZI and Pde11a-positive neurons in the medial ZI displayed distinct efferent projections

Previous studies showed that GABAergic neurons in the ZI projected to different brain regions and exhibited various behavioral functions[30, 31]. We hypothesized that GABAergic projection neurons in different subregions of the ZI may drive distinct functions. Firstly, we further confirmed that *Ecel1* and *Pde11a* are co-expressed with GABAergic neuronal marker *Slc32a1* (Vgat, vesicular GABA transporter) in the ZIr (*Ecel1*$^+$*Slc32a1*$^+$ */Ecel1*$^+$*:* 96.39 ± 1.19%; *Ecel1*$^+$*Slc32a1*$^+$*/Slc32a1*$^+$: 59.69 ± 6.28%) and the ZIm (*Pde11a*$^+$*Slc32a1*$^+$*/Pde11a*$^+$: 100 ± 0.00%*; Pde11a*$^+$*Slc32a1*$^+$*/Slc32a1*$^+$: 33.92 ± 9.67%, n = 9 brain slices from 3 mice per group. Fig. 3a-c). And for selectively target of GABAergic projection neuron subtypes in the rostral or medial ZI, we constructed two transgenic mice to selectively label *Ecel1*-expressing neurons (Ecel1-Cre) and *Pde11a*-expressing neurons (Pde11a-Cre), respectively (Fig. 3d). We verified the specificity of transgenic mice by examining the co-expression of Cre recombinase with *Ecel1* or *Pde11a*. The Cre recombinase expression in Ecel1-Cre is predominantly distributed in the ZIr (71.95 ± 1.12%, n = 9 brain slices from 3 mice) and highly co-expressed with *Ecel1* in ZIr (93.87 ± 1.45% *Ecel1*$^+$Cre$^+$ double positive neurons out of Cre$^+$ neurons. 96.41 ± 0.92% *Ecel1*$^+$Cre$^+$ double positive neurons out of *Ecel1*$^+$ neurons). In contrast, the expression of Cre recombinase in Pde11a-Cre mice is predominantly distributed in the ZIm (90.33 ± 2.91%, n = 9 brain slices from 3 mice) and highly co-expressed with *Pde11a* (99.70 ± 0.15% *Pde11a*$^+$Cre$^+$ double positive neurons out of Cre$^+$ neurons, 98.91 ± 0.22% *Pde11a*$^+$Cre$^+$ double positive neurons out of *Pde11a*$^+$ neurons. Fig. 3e-i). These results demonstrated high fidelity of selective labeling of *Ecel1* and *Pde11a*-expressing neurons by the Ecel1-Cre and Pde11a-Cre transgenic mice.

Next, we examined the axonal projections of ZIr^{Ecel1} and ZIm^{Pde11a} GABAergic neurons by stereotaxic injection of AAV virus carrying Cre-dependent expression

of membrane-bound GFP (mGFP) and synaptophysin-mRuby (SYP-mRuby) (Fig. 4a, b and Supplementary Fig. 3a, b). We found the axon terminals of ZIr^{Ecel1} GABAergic projection neurons distributed in several brain regions including periaqueductal gray (PAG), lateral septal nucleus (LS), preoptic area (POA), paraventricular nucleus of the thalamus (PVT), reuniens thalamic nucleus (Re), lateral hypothalamic area (LH), mediodorsal thalamic nucleus (MD) (Fig. 4c-e and Supplementary Fig. 3c). In contrast, the axon terminals of ZIm^{Pde11a} GABAergic neurons distributed in brain regions including pontine reticular formation (PRF), posterior complex of the thalamus (PO), auditory cortex (AuV), anterior pretectal nucleus, dorsal part (APTD), nucleus of Darkschewitsch (Dk), red nucleus (RN) and superior colliculus (SC) (Fig. 4c-e and Supplementary Fig. 3c). These results demonstrated divergent efferent projections of ZIr^{Ecel1} and ZIm^{Pde11a} GABAergic neurons to distinct downstream brain regions. For example, the periaqueductal gray (PAG) received extensive axonal projections from ZIr^{Ecel1} neurons (ZIr^{Ecel1}-PAG pathway), but very few projections from ZIm^{Pde11a} neurons. In contrast, pontine reticular formation (PRF) received axonal projections predominantly from ZIm^{Pde11a} (ZIm^{Pde11a}-PRF pathway), but not ZIr^{Ecel1} GABAergic neurons (Fig. 4c, d). Therefore, the efferent projection of ZIr^{Ecel1} and ZIm^{Pde11a} GABAergic neurons to different downstream target brain regions may imply their distinct behavioral functions.

Activation of ZIr^{Ecel1} neurons and the GABAergic projection from ZIr^{Ecel1} to PAG pathway mediates self-grooming

To investigate the behavioral function of ZIr^{Ecel1} GABAergic projection neurons, we bilaterally injected AAV virus expressing Cre-dependent channelrhodopsin2-EYFP (AAV-DIO-ChR2-EYFP) or EGFP as control (AAV-DIO-EGFP) into the ZIr of Ecel1-Cre mice (Fig. 5a and Supplementary Fig. 4a). We found optogenetic activation of ChR2-expressing ZIr^{Ecel1} GABAergic neurons at different stimulation frequencies (5Hz, 10Hz, 20Hz) elicited robust self-grooming behavior compared with EGFP-expressing control mice (Fig. 5b-d, Supplementary Fig. 4b,c and Supplementary Video 1 and 2). High frequency optogenetic stimulation (20 Hz)

229 also increased food intake or gnawing behavior (Supplementary Fig. 5a-d and
230 Supplementary Video 3-6), consistent with previous findings on optogenetic
231 activation of GABAergic neurons in the rostral ZI[34]. Self-grooming is reported to be
232 associated with stress[52, 53], increased anxiety[54-56] or reward behaviors[57, 58]. We
233 further measured the Ecel1-Cre mice in real time place preference test (RTPP)
234 and found that optogenetic activation of ZIr^{Ecel1} neurons resulted in aversion to the
235 optogenetic stimulation paired side (Supplementary Fig. 6e-g). These results
236 indicate that ZIr^{Ecel1} neurons mediate self-grooming behaviors could be associated
237 with negative emotion.

238 Next, we examined the downstream brain region of ZIr^{Ecel1} neurons that
239 mediated self-grooming behavior. Our results showed the axonal projection
240 terminals in periaqueductal gray (PAG) from ZIr^{Ecel1} GABAergic neurons (Fig. 4c).
241 The PAG neurons are reported to be an important sensory processing area which
242 also involved in the regulation of self-grooming[54, 58], different behaviors could be
243 mediated by distinct neuron subtypes or ensembles of neurons driven by different
244 descending afferents. To investigate whether the ZIr^{Ecel1} to PAG pathway mediate
245 self-grooming, we bilaterally injected AAV-DIO-ChR2-EYFP or AAV-DIO-EGFP
246 into the ZIr of Ecel1-Cre mice (Fig. 5h and Supplementary Fig. 7). We first
247 examined the functional synaptic connection from the ZIr^{Ecel1} to PAG pathway by
248 whole-cell patch-clamp recording of PAG neurons (Fig. 5e). We found that
249 optogenetic stimulation of axon terminals from ZIr^{Ecel1} GABAergic neurons induced
250 evoked inhibitory postsynaptic currents (IPSCs) in the PAG neurons in acute brain
251 slices, that could be completely blocked by the $GABA_A$ receptor antagonist
252 bicuculline (20 μM). Administration of the Na^+ channel inhibitor tetrodotoxin (TTX,
253 1 μM) blocked the optogenetically evoked IPSCs, while subsequent application of
254 the K^+ channel blocker 4-aminopyridine (4-AP, 100 μM) restored the evoked IPSCs
255 (Fig. 5f, g). These results demonstrated functional monosynaptic GABAergic
256 synaptic inputs from ZIr^{Ecel1} GABAergic neurons to the PAG.

257 In addition, we investigated the behavioral function of the ZIr^{Ecel1} to PAG
258 pathway. We found optogenetic activation of the ChR2-expressing axon terminals

from ZIr^{Ecel1} neurons to the PAG significantly induced increase in self-grooming time and grooming bouts (Fig. 5i, j). We also examined whether optogenetic stimulation of axonal projections from ZIr^{Ecel1} neurons to other target brain regions could induce self-grooming behavior. We found that optogenetic activation of the ChR2-expressing axon terminals from ZIr^{Ecel1} neurons to other targets including LS, POA, LH or SC had no discernible impact on either self-grooming time or self-grooming bouts in ChR2-group compared with EGFP-group (Supplementary Fig. 8). Together, these results demonstrate that activation of the ZIr^{Ecel1} neurons and the GABAergic projection from ZIr^{Ecel1} to PAG pathway mediates self-grooming behavior.

ZIr^{Ecel1} neurons bidirectionally regulate self-grooming behavior

To monitor the activity of ZIr^{Ecel1} GABAergic neurons during self-grooming *in vivo,* we unilaterally injected AAV virus expressing Cre-dependent GCaMP6s and mCherry (as control) in the ZIr of Ecel1-Cre mice and recorded the calcium activity by fiber photometry (Fig. 6a, b). The self-grooming behavior can be efficiently induced by water spray toward the face[52, 58, 59], we found the grooming time increased significantly compared to that before the water spray treatment (Fig. 6c, d). The calcium fluorescent signal of ZIr^{Ecel1} neurons increased before the start of grooming but decreased throughout the entire self-grooming period, and then returned to baseline after termination of self-grooming during both water spray induced and spontaneous self-grooming (Fig. 6e-g and Supplementary Fig. 9a-f). These results suggest that the increased activity of ZIr^{Ecel1} GABAergic neurons preceded the self-grooming behavior[53, 60].

We further chemogenetically activated or inhibited the ZIr^{Ecel1} neurons by bilaterally injecting AAV-DIO-hM3Dq-mCherry or AAV-DIO-hM4Di-mCherry (or AAV-DIO-mCherry as control) into the ZIr of Ecel1-Cre mice (Fig. 7a, e). We found that chemogenetic activation of ZIr^{Ecel1} neurons significantly increased the self-grooming time and self-grooming bouts in hM3Dq-expressing mice compared with the mCherry-expressing control mice (Fig. 7b-d and Supplementary Fig. 9g), but chemogenetic inhibition of ZIr^{Ecel1} neurons showed no discernable effect on the

spontaneous self-grooming behavior in hM4Di-expressing mice compared with the mCherry-expressing control mice (Supplementary Fig. 9h and i). To test whether ZIr^{Ecel1} neurons are required for water spray induced self-grooming behavior, the mice were i.p. administered with CNO (3 mg/kg) 30 min before water spray toward the mice face following by 20min self-grooming test (Fig. 7f). We demonstrated that chemogenetic inhibition of Ecel1 positive neurons in the ZIr significantly decreased the total self-grooming time and self-grooming bout duration in hM4Di-expressing mice compared with the mCherry-expressing control mice in water spray induced self-grooming (Fig. 7g-i and Supplementary Fig. 9k). Moreover, we further ablated the ZIr^{Ecel1} neurons by bilaterally injected AAV virus carrying Cre-dependent DTA (AAV-DIO-DTA) or mCherry (AAV-DIO-mCherry) as control into the ZIr of Ecel1-Cre mice (Fig. 7j and Supplementary Fig. 9l-n). While ablation of ZIr^{Ecel1} neurons showed no discernable effect on the spontaneous self-grooming behavior (Supplementary Fig. 9j), we found that ablation of ZIr^{Ecel1} neurons also significantly reduced the self-grooming time and grooming bouts induced by water spray in DTA-expressing mice compared with the mCherry-expressing control mice (Fig. 7k-m). These results indicates that the ZIr^{Ecel1} neurons can bidirectionally regulate the self-grooming behavior.

Activation of ZIm^{Pde11a} neurons and the GABAergic projection from ZIm^{Pde11a} to PRF pathway promotes transition from sleep to wakefulness

We next investigated the behavioral function of ZIm^{Pde11a} GABAergic neurons by injecting AAV-DIO-ChR2-EYFP or control AAV-DIO-EGFP virus into the ZIm of Pde11a-Cre mice (Supplementary Fig. 10a). Optogenetic activation of ZIm^{Pde11a} neurons during the awake state of mice did not have significant impact on the center time or locomotor activity in open field test, or the time spent in open arm in EPM test, or preference to light stimulation in RTPP test (Supplementary Fig. 10f-l). Our result showed extensive axonal projections from the ZIm^{Pde11a} neurons to the oral part of pontine reticular formation (PRF) (Fig. 4c), which is a component of the ascending reticular activating system that modulates rapid eye movement

319 sleep (REM) in sleep and wakefulness cycle[61, 62]. To investigate whether ZIm^{Pde11a}
320 GABAergic projection neurons participated in regulating sleep-wakefulness cycle,
321 we monitored the activity of ZIm^{Pde11a} neurons by AAV mediated Cre-dependent
322 expression of GCaMP6s or mCherry (as control) using fiber photometry. The
323 phase of sleep-wakefulness cycle was determined by electroencephalogram
324 (EEG) and electromyogram (EMG) recordings (Fig. 8a, b). We found the ZIm^{Pde11a}
325 neurons are active during REM sleep and wakefulness, the calcium signal
326 increases during the transition from NREM to REM sleep and decreases during
327 the transition from REM sleep to wakefulness and wakefulness to NREM sleep
328 (Fig. 8c-e).

329 Optogenetic activation of ChR2-expressing ZIm^{Pde11a} GABAergic projection
330 neurons promotes the transition from NREM or REM sleep to wakefulness in
331 comparison with the EGFP control group (20 Hz, 120 seconds per trial, applied
332 every 10–15 minutes. Fig. 9a-d and Supplementary Video 7 and 8). The transition
333 probability from REM sleep to wakefulness and NREM sleep to wakefulness was
334 significantly increased upon optogenetic activation of the ZIm^{Pde11a} GABAergic
335 projection neurons, along with a complementary decrease of transition probability
336 from wakefulness to NREM or NREM to REM sleep (Fig. 9e and Supplementary
337 Fig. 10b-e). We verified the functional synaptic connectivity from ZIm^{Pde11a} to PRF
338 pathway by whole-cell patch-clamp recording of neurons in the PRF (Fig. 9f).
339 Optogenetic stimulation of the ChR2-expressing axonal terminals from ZIm^{Pde11a}
340 neurons evoked IPSCs in PRF neurons that can be blocked by bicuculline (20 μM)
341 or TTX (1 μM). The blockade of IPSCs by TTX was restored following application
342 of 4-AP (100 μM), suggesting monosynaptic GABAergic inputs from ZIm^{Pde11a} to
343 PRF pathway (Fig. 9g, h). We investigated the behavioral function of the ZIm^{Pde11a}
344 to PRF pathway and found optogenetic activation of the GABAergic projections
345 from ZIm^{Pde11a} to the PRF increased the transition probability from NREM to
346 wakefulness and decreased the transition probability from wakefulness to NREM
347 or from NREM to REM sleep (Fig. 9i-l and Supplementary Fig. 11). Thus, these
348 results demonstrate that activation of the ZIm^{Pde11a} GABAergic projection neurons
349 and the ZIm^{Pde11a} to PRF pathway promotes transition from sleep to wakefulness.

ZIm^{Pde11a} neurons bidirectionally regulate sleep-wakefulness cycle

We further chemogenetically activated ZIm^{Pde11a} neurons by bilaterally injecting AAV-DIO-hM3Dq-mCherry or AAV-DIO-mCherry as control into the ZIm of Pde11a-Cre mice (Fig. 10a). We found that chemogenetic activation of ZIm^{Pde11a} neurons significantly increased wakefulness and decreased NREM and REM sleep in hM3Dq-expressing mice following CNO injection compared with saline injection group during the light phase (Fig. 10b-h). In addition, the number of episodes during wakefulness and NREM both increases, but the duration of average NREM episode significantly decreases, suggesting chemogenetic activation of ZIm^{Pde11a} neurons increased wakefulness at the expense of sleep time and sleep quality in the light phase (Fig. 10i, j). Chemogenetic inhibition did not alter the sleep-wakefulness state in hM4Di-expressing mice or in mCherry-expressing control mice (Supplementary Fig. 12a-h). To determine whether ZIm^{Pde11a} neurons are required for sleep-wakefulness transition, we selectively ablated the ZIm^{Pde11a} neurons by bilaterally injected AAV-DIO-DTA or AAV-DIO-mCherry as control into the ZIm of Pde11a-Cre mice (Fig. 10k) and verified the efficiency of DTA ablation (Supplementary Fig. 12i-k). We found that ablation of ZIm^{Pde11a} neurons significantly decreased wakefulness and increased the NREM and REM sleep during dark phase (Fig. 10l-q). In addition, the number of episodes during wakefulness, NREM and REM all increases, but the duration of average wakefulness episode significantly decreases, suggesting ZIm^{Pde11a} neurons may be required for wakefulness in the dark phase (Fig. 10r, s). These results demonstrate that the ZIm^{Pde11a} neurons can bidirectionally regulate the sleep and wakefulness cycle.

We further explored whether ZIr^{Ecel1} and ZIm^{Pde11a} neurons play distinct roles in regulating self-grooming or sleep-wakefulness cycle behaviors. We found that ablation of the ZIm^{Pde11a} neurons by selective expression of DTA had no effects on the spontaneous or water spray induced self-grooming behaviors compared with mCherry control group (Supplementary Fig. 13j-m). Additionally, ablation of ZIr^{Ecel1} neurons by DTA had no significant impact on the time or episodes of wakefulness,

NREM sleep or REM sleep compared with mCherry-group mice (Supplementary Fig. 13a-i). These results suggest that these ZIr^{Ecel1} and ZIm^{Pde11a} neurons differentially regulate self-grooming or sleep-wakefulness cycle behaviors, respectively.

Taken together, our study revealed the molecular markers and spatial distribution of GABAergic neuron subtypes in subregions of zona incerta. By *in vivo* circuit mapping and manipulating the neuronal activity, we further delineated distinct functions for two discrete GABAergic projection neuron subtypes: the ZIr^{Ecel1} GABAergic neurons regulate self-grooming through projection to PAG pathway and ZIm^{Pde11a} GABAergic neurons promote transition from sleep to wakefulness through projection to PRF pathway. These results demonstrated the molecular markers, spatial distribution and circuit mechanisms of GABAergic projection neuron subtypes in the ZI that mediate distinct innate behaviors.

Discussion

Molecular markers and spatial localization of GABAergic projection neuron subtypes in zona incerta

Despite the unique long-range axonal projection pattern and distinct functions of GABAergic projection neurons, the lack of specific molecular markers makes it difficult to selectively target or to investigate the function of GABAergic projection neurons *in vivo*. By single-nucleus transcriptomic sequencing of the ZI and quantifying the spatial expression of marker genes of GABAergic neurons in different subregions along the anteroposterior axis of the ZI, we found two discrete *Ecel1*- and *Pde11a*-expressing GABAergic neurons that are non-overlapping and exhibit dominant expression in the rostral and medial ZI, respectively (Fig. 2d, e).

By *in vivo* circuit mapping, we further demonstrated that ZIr^{Ecel1} and ZIm^{Pde11a} neurons sent long-range GABAergic efferent projections to segregated distant brain regions in the forebrain and the midbrain (Fig. 4 and Supplementary Fig. 3c),

implying distinct behavioral functions. We also found the axonal projections from the ZIm^{Pde11a} GABAergic projection neurons to the layer 1 of auditory cortex (Supplementary Fig. 3c), consistent with recent finding reporting the top-down GABAergic projection from ZI in regulating neocortical associative fear learning[27]. The establishment and maintenance of specific projections are determined by both genetic and environmental factors[63-65]. Recent studies showed heterogeneity of the projection area and potential functions in transcriptomic neuron subtypes[66]. Therefore, the same transcriptomic neuronal subtypes could establish different efferent projections during development[66]. The diverse behavioral functions of the ZI are routed in the heterogenous neuron populations, that are possibly generated from different progenitor cells during development[67, 68]. Future studies are warranted to elucidate the developmental origin of GABAergic neuron subtypes in the ZI.

Activation of ZIr^{Ecel1} GABAergic projection neurons induced self-grooming behaviors may be associated with stress

Previous reports suggested that ZI neurons could receive information from different sensory modalities including auditory, whisker and visual stimulation[31, 37, 69]. By monitoring the calcium dynamics of ZIr^{Ecel1} neurons *in vivo*, we found increased calcium activity of ZIr^{Ecel1} neurons before water spray induced self-grooming, suggesting these neurons could be activated by water spray induced unpleasant sensory stress[52, 59] (Fig. 6). Chemogenetic inhibition or ablation of ZIr^{Ecel1} neurons impaired the self-grooming behavior induced by water spray but had little effect on the spontaneous self-grooming behavior (Fig. 7e-m and Supplementary Fig. 9h-j). Thus, these results suggest that activation of ZIr^{Ecel1} neurons induced self-grooming behaviors could be associated with sensory stress.

Self-grooming is an innate behavior that could be elicited by comfort or stressful conditions[70]. Our results demonstrated that optogenetic activation of ZIr^{Ecel1} neurons increased the bouts of self-grooming and induced aversion to laser

stimulation paired side (Fig. 5a-d and Supplementary Fig. 6e-g), resembling with stress-associated self-grooming behavior that often accompanied by negative emotional state[52, 59]. Previous study showed that activation of somatostatin (SST)-expressing neurons or calretinin (CR)-expressing neurons in the ZI differentially modulate anxiety[40]. We found that only subsets of *Ecel1*-expressing neurons co-expressed *SOM* (*Ecel1*$^+$*SST*$^+$/*Ecel1*$^+$, 23.12 ± 1.12%; *Ecel1*$^+$*SST*$^+$/*SST*$^+$, 33.93 ± 0.96%), while *Ecel1*-expressing neurons rarely co-expressed *CR* in the rostral ZI (*Ecel1*$^+$CR$^+$/*Ecel1*$^+$, 4.10 ± 0.15%; *Ecel1*$^+$CR$^+$/CR$^+$, 13.80 ± 2.38%. Supplementary Fig. 14). In addition, optogenetic stimulation of ZIr^{Ecel1} neurons did not affect the center time in open field behavioral test, or time spent in the open arm in elevated plus maze (EPM) behavioral test (Supplementary Fig. 6a-d), or the time of investigating the novel object compared with familiar object in novel object recognition test (Supplementary Fig. 6h, i). Together, these results suggest that ZIr^{Ecel1} neurons could be a distinct subpopulation of GABAergic projection neurons that mediated stress-related self-grooming behavior.

Stress may lead to decreased feeding and increased grooming[71, 72]. Previous studies demonstrated that hypothalamic neuronal circuit can exert scalable control over feeding and negative emotional states[52]. Our results showed that low frequency optogenetic stimulation (5Hz) of ZIr^{Ecel1} neurons only promote self-grooming, while high frequency optogenetic stimulation (20Hz) of ZIr^{Ecel1} neurons also increased feeding, suggesting ZIr^{Ecel1} neurons may orchestrate behaviors related to stress response and feeding (Fig. 5b-d, Supplementary Fig. 4b,c and Supplementary Fig. 5a-d). In addition, we found ablation of ZIr^{Ecel1} neurons significantly reduced water spray induced self-grooming (Fig. 7j-m), but had no discernible impact on food intake or the body weight (Supplementary Fig. 5e-h). These results demonstrate that ZIr^{Ecel1} neurons are required for sensory stress related self-grooming.

ZIm^{Pde11a} GABAergic projection neurons participate in regulating sleep-wakefulness cycle

467 Extensive GABAergic projections from the diencephalon including ZI, reticular
468 thalamus and hypothalamus to pontine reticular formation (PRF) have been
469 identified by retrograde tracing approaches[73]. Endogenous GABA levels were
470 increased during wakefulness and application of $GABA_A$ receptor agonists in PRF
471 promotes wakefulness[74-76]. We demonstrated that activation of ZIm^{Pde11a} neurons
472 and the GABAergic projection from ZIm^{Pde11a} to PRF promote the transition from
473 sleep to wakefulness (Fig. 9). We found increased Ca^{2+} activity of ZIm^{Pde11a}
474 neurons during REM sleep and in wakefulness using fiber photometry recordings
475 (Fig. 8). Recent studies using *in vivo* micro-endoscopic imaging showed that
476 GABAergic neurons in the ZI demonstrated heterogenous activity in sleep-
477 wakefulness cycle, including neurons showing maximal Ca^{2+} activity during REM
478 sleep (REM-active), neurons showing maximal Ca^{2+} activity during wakefulness
479 (Wake-active), or neurons showing Ca^{2+} activity in both REM sleep and
480 wakefulness (Wake/REM-active)[77].

481 Activation of REM-active neurons promote REM sleep, often at the expense
482 of NREM sleep[78, 79], while activation of Wake/REM-active neurons (arousal
483 neurons) promote wakefulness[80-82]. The ZIm^{Pde11a} neurons may include both REM-
484 active and Wake/REM-active neurons as demonstrated by fiber photometry
485 recording (Fig. 8). Therefore, optogenetic stimulation of ZIm^{Pde11a} neurons
486 promotes the transition from sleep to wakefulness could be mediated by the
487 activation of the Wake/REM-active ZIm^{Pde11a} neurons. Additionally, optogenetic
488 activation of ZIm^{Pde11a} neurons decreased the investigating time of both familiar
489 and novel object compared with control group in the novel object recognition test,
490 (Supplementary Fig. 10m,n), suggesting a potential shift to alert state during
491 wakefulness[83, 84].

492 The zona incerta has been a target for chronic deep brain stimulation in
493 treating Parkinson's disease (PD)[85, 86]. Previous studies reported activation of
494 Lhx6-expressing GABAergic neurons subtypes induced transition from
495 wakefulness to sleep[35]. Our results showed that *Pde11a*-positive neurons rarely
496 co-expressed with *Lhx6* (*Pde11a*$^+$*Lhx6*$^+$/*Pde11a*$^+$, 2.23 ± 1.18%;

Pde11a^{+}*Lhx6*$^{+}$/*Lhx6*$^{+}$, 1.38 ± 0.69%, n = 6 brain slices from 3 mice. Supplementary Fig. 15), suggesting ZIm^{Pde11a} is a distinct GABAergic projection neuron subpopulation that promote the transition from sleep to wakefulness. These findings demonstrate that *Pde11a*$^{+}$ and *Lhx6*$^{+}$ neuronal subpopulations in the ZIm may differentially regulate sleep-wakefulness cycle. Intriguingly, sleep abnormalities are reported in Parkinson's patients and in rodent models of PD[87, 88], it is plausible that chronic deep brain stimulation of ZI may help improve sleep-related symptoms in Parkinson's disease. Future studies are warranted to further elucidate the subtype and the exact role of GABAergic neurons in regulating sleep disturbances.

In summary, our results revealed the spatial distribution of two discrete populations of GABAergic projection neurons in segregated subregions of the ZI. By constructing transgenic mice to selectively target the ZIr^{Ecel1} and ZIm^{Pde11a} GABAergic projection neurons, we further demonstrated their efferent axonal projection to non-overlapping distant brain regions and mediate distinct innate behavioral functions. These findings uncovered the molecular markers, spatial organization and functions for GABAergic projection neuron subtypes in the zona incerta that play distinct roles in regulating self-grooming and sleep-wakefulness cycle.

Methods

Animals

All experiments were conducted in accordance with the guidelines of Zhejiang University (ZJU) and were approved by the Animal Advisory Committee at ZJU. Wild-type C57BL/6J (JAX# Stock No. 000664) and transgenic GAD67-GFP mice (JAX# Stock No. 007677) were obtained from Jackson Laboratories. Transgenic mice Ecel1-Cre and Pde11a-Cre (C57/BL6 background) were generated by CRISPR/Cas9 technology at the Shanghai Model Organisms Center (China) or Biocytogen (Beijing) company. All mice were bred and housed at the temperature

(23 ± 1 °C) and humidity (40%) controlled animal facility at ZJU under a 12 h light/dark cycle with light on at zeitgeber time 0 (ZT 0; 7:00), food and water were available ad libitum. Only adult (>8 weeks old) mice of normal appearance and weight were used for behavioral tests. Littermate mice were split into random groups before AAV viral injection.

Viruses

AAV2/9-DIO-mGFP-Synaptophysin-mRuby (titer: 8.9×10^{12} genomic copies per ml), AAV2/9-EF1α-DIO-hChR2-EYFP (titer: 2×10^{12} genomic copies per ml) were purchased from Taitool Bioscience, China. AAV2/9-hSyn-DIO-EGFP (titer: 1.44×10^{12} genomic copies per ml) were purchased from WZ Bioscience, China. AAV2/9-EF1α-DIO-GCamP6s (titer: 8.35×10^{12} genomic copies per ml). AAV2/9-CAG-DIO-DTA (titer: 6.13×10^{12} genomic copies per ml). AAV2/9-DIO-mCherry (titer: 5.48×10^{12} genomic copies per ml) were purchased from BrainVTA Bioscience, China. AAV2/9-hSyn-DIO-hM3Dq-mCherry (titer: 3.27×10^{13} genomic copies per ml). AAV2/9-hSyn-DIO-hM4Di-mCherry (titer: 8.53×10^{13} genomic copies per ml) were purchased from Sunbio Medical Biotechnology Company, China.

Stereotaxic injection

Adult mice were anesthetized with pentobarbital sodium solution (50 mg/kg) via an intraperitoneal (i.p.) injection. Mice were placed on a stereotaxic frame (RWD Life Science, 68046) and anesthesia were maintained with 1%-1.5% isoflurane during surgery. Injection of AAV virus was performed with a manual viral syringe pump connected to glass micropipette with a 10-50 μm diameter tip (Drummond Scientific Company, Wiretrol II). After each injection, the syringe was left *in situ* for an additional 10 min and then withdrawn slowly. Mice were randomly assigned to experimental and control groups before virus injection.

553 To map the axonal projection pattern of GABAergic neurons in the rostral or
554 medial zona incerta, anterograde tracing virus AAV2/9-DIO-mGFP-
555 Synaptophysin-mRuby (80 nl. nl: nano-liter) was unilaterally injected into the ZIr
556 (anteroposterior (AP): −1.00 mm, mediolateral (ML): −0.60 mm, dorsoventral (DV):
557 −4.45 mm) of Ecel1-Cre mice or the ZIm (AP: −2.30 mm, ML: −1.50 mm, DV: −4.20
558 mm) of Pde11a-Cre mice. Three weeks after injection, mice were sacrificed and
559 brain sections were collected for fluorescent imaging. The projection pattern was
560 shown as the percentage of total relative fluorescent density occupied by different
561 downstream brain areas.

562 The neuronal activity of GABAergic neurons was monitored by in *vivo* fiber
563 photometry recording. AAV2/9-EF1α-DIO-GCamP6s and AAV2/9-DIO-mCherry
564 were injected as a mixture at 2:1 ratio (80 nl) into the ZIr of Ecel1-Cre mice or ZIm
565 of Pde11a-Cre mice. Three weeks after injection, optical fibers (200 μm O.D., 0.37
566 NA, Inper, Hangzhou, China) were implanted above the ZIr in Ecel1-Cre mice or
567 ZIm in Pde11a-Cre mice, respectively.

568 To activate GABAergic neuron subtypes by in *vivo* optogenetic stimulation,
569 AAV2/9-EF1α-DIO-hChR2-EYFP or AAV2/9-hSyn-DIO-EGFP (80 nl) were
570 bilaterally injected into the ZIr of Ecel1-Cre mice or unilaterally injected into the
571 ZIm of Pde11a-Cre mice. Three weeks after injection, optical fibers were implanted
572 at a 10° angle relative to the vertical plane above ZIr bilaterally (AP: −1.00 mm;
573 ML: ±1.35 mm; DV: −4.13 mm) in Ecel1-Cre mice. The optical fibers were
574 unilaterally implanted 100 μm above viral injection coordinates of the ZIm in
575 Pde11a-Cre mice. The optical fibers were implanted at a 10° angle relative to the
576 vertical plane above PAG bilaterally in Ecel1-Cre mice (AP: −4.40 mm; ML: ±1.00
577 mm; DV: −2.15 mm) to optogenetically stimulate axon terminals from ZIr to PAG.
578 The optical fibers were unilaterally implanted into the PRF in Pde11a-Cre mice
579 (AP: −4.4 mm; ML: ±0.85 mm; DV: −4.6 mm) to optogenetically stimulate axon
580 terminals from ZIm to PRF.

581 To chemogenetic manipulation of GABAergic neuron subtypes, AAV2/9-hSyn-
582 DIO-hM3Dq-mCherry or AAV2/9-hSyn-DIO-hM4Di-mCherry (80 nl) were

bilaterally injected into the ZIr of Ecel1-Cre mice or ZIm of Pde11a-Cre mice. For the DTA mediated ablation experiments, AAV2/9-CAG-DIO-DTA (80nl) were bilaterally injected into the ZIr of Ecel1-Cre mice or ZIm of Pde11a-Cre mice.

Dual color fiber photometry

Calcium signals were recorded using a dual-color fiber photometry system (Thinkertech, Nanjing Bioscience Inc.). GCamP6s was excited by 488 channels to record changes of calcium activity, and mCherry fluorescent signal was excited by 570 nm channel as control to exclude disturbances of fluorescent signals caused by artificial factors. The laser power at the tip of the optical fiber was adjusted to be 30 μW for 488 nm excitation channel and 10 μW for the control channel (570 nm) to decrease laser bleaching of fluorescent signals. Averaged traces of Ca^{2+} fluorescent signal changes and heatmap were plotted using the MATLAB program provided by ThinkerTech Nanjing Bioscience. Adult male mice were used for dual color fiber photometry.

***In vivo* optogenetic manipulation**

Mice were recovered for at least 1 week after optical fiber implantation surgery. For optogenetic manipulation during the behavioral assessments, pulses of 465 nm laser stimulation were set by laser stimulator (INPER-B1-465, Inper, Hangzhou, China). Before behavioral tests, mice were habituated to the environments for at least 30 min after connection to a laser stimulator. The laser power at the tip of the optical fiber was adjusted to 5-10 mW for the optogenetic stimulation (10 ms pulses at 20 Hz or 5Hz). Adult male mice were used for optogenetic manipulation.

Electrophysiology

Mice were anesthetized with pentobarbital sodium solution (50 mg/kg) via intraperitoneal injection (i.p.) and then the brains were removed and placed into ice-cold oxygenated artificial cerebrospinal fluid (ACSF) containing (in mM) 110 Choline chloride, 2.5 KCl, 0.5 $CaCl_2$, 7 $MgCl_2$, 1.3 NaH_2PO_4, 25 $NaHCO_3$, 20 Glucose, 1.3 Na-Ascorbate, 0.6 Na-Pyruvate. Coronal brain slice sections (300 μm thickness) including the periaqueductal gray (PAG) or sagittal sections (250 μm thickness) including the pontine reticular formation (PRF) region were made on a vibratome (VT1200S, Leica) in ice-cold ACSF. The brain slices were incubated at 30 ± 2 ℃ for 0.5 hour and recovered for 1 hour at room temperature in a recording solution containing (in mM) 125 NaCl, 2.5 KCl, 2 $CaCl_2$, 7 $MgCl_2$, 1.3 NaH_2PO_4, 25 $NaHCO_3$, 10 Glucose, 1.3 Na-Ascorbate, 0.6 Na-Pyruvate. After recovering, individual brain slices were transferred to the recording chamber and continuously perfused (2 – 4 ml/min) with ACSF containing (in mM) 125 NaCl, 2.5 KCl, 2 $CaCl_2$, 7 $MgCl_2$, 1.3 NaH_2PO_4, 25 $NaHCO_3$, 10 Glucose. The incubating and recording ACSF solutions were continuously bubbled with 95% O_2/5% CO_2.

To test the monosynaptic and inhibitory connection of the ZIr to PAG or the ZIm to PRF, light-evoked inhibitory postsynaptic currents (eIPSCs) were recorded using pipettes (3 - 5 MΩ) filled with inner solution containing 133 $CsMeSO_4$, 7 CsCl, 10 HEPES, 4 $MgCl_2$, 0.5 EGTA, 3 CsOH, 4 Na_2ATP, 0.4 Na_4GTP, 5 QX-314 (PH 7.35; Osmolarity 310 ± 10 mOsm). And TTX (1 μM, Absin, China) was used to block the sodium channel and followed by the 4-AP (100 μM) to confirm the monosynaptic postsynaptic currents following light activation. Bicuculine (20 μM, Abcam, UK) was bath applied to validate whether the recorded IPSCs were mediated by GABA receptors. Whole-cell patch-clamp recordings were conducted with Multiclamp 700B amplifier (Axon) controlled by DigiData 1550B digitizer and analyzed with pClamp (Clampex, Clampfit, v10.7). Both male and female mice were used for electrophysiology.

Nuclei isolation and single-nuclei RNA sequencing analysis

638 Sagittal brain slice sections (600 μm) from Gad67-GFP knock-in mice at postnatal
639 day 40 (P40) were made with a vibratome as described above. The zona incerta
640 region indicated by expression of fluorescent reporters were microdissected under
641 a fluorescence stereomicroscope (Leica VT1200S, Germany) and collected in ice-
642 cold artificial cerebrospinal fluid (ACSF). Two independent cohort of micro-
643 dissected zona incerta brain slice sections (each cohort were collected from 3 male
644 mice and 3 female mice) were harvested for single-nuclei RNA sequencing.

645 Nuclei isolation from micro-dissected tissue was performed using the following
646 procedure: the collected tissue was homogenized in ice-cold RNAase-free
647 homogenization buffer[89] containing: 0.32 M sucrose, 5 mM $CaCl_2$, 3 mM $MgAC_2$,
648 0.1 mM EDTA (Invitrogen, AM9260G), 10 mM Tris-HCl pH 7.6 (Invitrogen, 15568-
649 025), 0.4 U/ul Recombinant RNA inhibitor (Takara, 2312A), 0.1 mM PMSF (Roche,
650 10837091001), 0.1 mM β-mercaptoethanol, 1% BSA, 0.01% 10% NP40 (Thermo,
651 85124) in UltraPure distilled-water. Subsequently 1.5 mL 0.32 M Sucrose solution
652 containing 0.32 M sucrose, 5 mM $CaCl_2$, 3 mM $MgAC_2$, 0.1 mM EDTA, 10 mM
653 Tris-HCl pH 7.6, 0.4 U/ul Recombinant RNA inhibitor, 0.1 mM β-mercaptoethanol,
654 1% BSA in UltraPure distilled-water were added to the homogenates, mixed well,
655 and centrifuged by 900 g for 10 min. After removing the supernatant, another 1.5
656 mL 0.32 M sucrose solution was added to the tube, resuspended, filtered by 35
657 μm cell-strainer (FALCON, 352235), and then centrifuged at 900 g for 8 min. The
658 precipitate was collected and resuspended in 1.5 mL 0.32 M sucrose solution and
659 was centrifuged at 600 g for two times. The precipitate was resuspended in 0.32
660 M sucrose solution and diluted with an equal volume of 50% OptiPrep density
661 gradient medium (60% OptiPrep density gradient medium, 0.32 M sucrose
662 solution) to give a final concentration of 25% medium solution. Slowly adding the
663 29% OptiPrep density gradient medium (60% OptiPrep density gradient medium,
664 0.32 M sucrose solution) under the 25% medium solution without disrupting the
665 layers in a 1.5 mL centrifuge tube and centrifuged by 3000 g for 20 min[90]. After the
666 removal of the supernatant, the nuclei pellet was dissolved in 100 μl PBS (Gibco,
667 10010-031). Nuclei density was analyzed using a cell counting plate (WATSON,
668 177-112C). Single nuclei capture was performed on 10X Genomics Single-Cell 3'

system with target capture of 8000 nuclei per sample. Single-nuclei libraries from individual samples were pulled and sequenced on the Illumina HiSeq X Ten machine. The 10x nuclei capture and library preparation protocol was performed according to the manufacturer's recommended protocol (10X Genomics).

Sequencing reads were aligned to mouse reference genome mm10 with CellRanger (version 6.0.2). Low abundant genes (expressed in less than 3 cells) and cells of potentially low quality (nFeature (number of detected genes) < 1000 or nFeature > 6,000, or counts > 25,000, or percentage of mitochondrial genes > 5%) were removed from downstream analysis. The generated gene expression matrix files arising from two batches of experiments were further analyzed using Seurat v4 package. Briefly, SCTransform normalization was performed and RPCA was used to integrate data. 3,000 variable genes were identified by FindVariableGenes and selected to function RunPCA for the principal component analysis (PCA). Next, Uniform Manifold Approximation and Projection (UMAP) was performed to reduce variation to two dimension and FindClusters was used for unsupervised clustering of cells by setting resolution to 0.6. Subsequently, canonical cell type-specific markers were used to annotate major cell types: neurons, oligodendrocytes, endothelial cells, astrocytes, oligodendrocyte progenitor cells (OPCs), pericytes, microglia, and differentiation-committed oligodendrocyte precursors (COPs). Furthermore, we reclustered excitatory neurons and inhibitory neurons into ten and twelve subclusters, respectively. The genes differentially expressed in cells of subclusters were analyzed using FindMarkers function and used the two-sided Wilcoxon Rank-Sum test (default). Those which with p value < 0.05 were selected as differentially expressed genes (DEGs) candidates. Heatmap showing differentially expressed genes was generated by ggplot2 package. The regional information of neuronal subclusters were determined by the expression of DEGs in brain slices from Allen Mouse Brain Atlas (https://mouse.brain-map.org).

Histology and immunofluorescent staining

Mice were deeply anesthetized with an intraperitoneal injection of pentobarbital sodium solution (50 mg/kg) and perfused transcardially with 0.1M phosphate-buffered saline (PBS, pH 7.4) followed by 4% paraformaldehyde (PFA). Brain tissues were collected and postfixed in 4% PFA for 6-8 hours at 4 °C. Fixed brains were then rehydrated with 28-30% sucrose in PBS at 4 °C for 48 hours. Subsequently, the brains were embedded with Optimal Cutting Temperature compound and were cut into 40 μm or 16 μm coronal sections using cryomicrotome (Thermo Scientific, CryoStar NX50). The brain slice sections were stored at -80 °C or in 0.01% sodium azide in PBS at 4 °C.

For immunofluorescent staining, brain sections were washed with 0.1M PBS for 3 times, 10 min each. Then sections were incubated with blocking buffer containing 10% donkey serum albumin (Jackson ImmunoResearch, USA) dissolved in 0.1% PBST (0.1% Triton X-100 in PBS) at room temperature for 1 hour. Sections were then incubated with primary antibody at 4 °C overnight. After washing in PBS, sections were incubated with secondary antibodies (1:1000, Invitrogen, USA) at room temperature for 1 hour. Finally, sections were mounted after counterstained with nuclear dye 4,6-diamidino-2-phenylindole (DAPI, Beyotime, China). All antibodies were titrated for working solution with blocking buffer. Primary antibody included anti-Cre recombinase (1:500, Synaptic Systems 257004, Germany) and anti-Calretinin (1:100, Swant CR6B3, Switzerland). Fluorescent images were taken with a confocal microscope (IX83-FV3000, Olympus, Japan) and a Virtual Slide Microscope VS120 (Olympus, Japan).

Fluorescence *in situ* hybridization (FISH) was performed according to the manufacture's protocol using RNAscope multiplex fluorescent reagent kit and following designed probes were used: RNAscope® Probe-Mm-Cdh23-C2, RNAscope® Probe-Mm-Ecel1-C3, RNAscope® Probe-Mm-Ptprk-C1, RNAscope® Probe-Mm-Pde11a-C1, RNAscope® Probe-Mm-Pax6-C2, RNAscope® Probe-Mm-Nos1-C3, RNAscope® Probe-Mm-Slc32a1-C4, RNAscope® Probe-Mm-Lhx6-C2, RNAscope® Probe-Mm-SST-C4 (Advanced Cell Diagnostics, USA). The density of marker genes was calculated as the cell numbers per μm2. The

distribution of marker genes was shown as the percentage of positive neuron numbers in different brain areas. Both male and female mice were used for immunofluorescent staining.

Behavioral analysis

Self-grooming measurement. Mouse self-grooming has a complex sequenced structure that consists of several syntactic chains which beginning from elliptical bilateral paw stroke (paw and nose grooming) to unilateral strokes from the mystacial vibrissae to face following by bilateral head grooming, and finally to body licking. A 350 mm × 350 mm square box was used for the self-grooming test. Mice were placed in the chamber to acclimate for at least 10 min before the behavioral tests. For the optogenetic manipulation, mice were placed in the center of the apparatus and the behavioral assay was performed with a 3-min Laser OFF, 3-min Laser ON and 3-min Laser OFF administration pattern. In the self-grooming test when optogenetic activation of Ecel1 positive neurons in the ZIr, different frequencies (1Hz, 5Hz, 10Hz and 20 Hz) were applied to ZIr. Self-grooming behavior was mort robustly induced when optogenetic stimulating Ecel1^{+} neurons in the ZIr at 5Hz, we therefore conducted the following experiments at 5Hz. For chemogenetic manipulation, mice was intraperitoneal administrated with clozapine-N-oxide (CNO, Sigma-Aldrich; 1 mg/kg in saline for hM3Dq-mediated activation and 3 mg/kg in saline for hM4Di-mediated inhibition) 30min before self-grooming test. For water spray in chemogenetic manipulation and DTA ablation experiments, water spray was started by spraying with water toward the face of mice 4 times with a sprayer and following with a 20min recording. The total time spent in self-grooming, self-grooming bouts and duration of self-grooming per bout were measured during the following 20min.

Open field test. A 450 mm × 450 mm square box was used for the open-field test. Mice were placed in the experimental room to acclimate for at least 30 min before the behavioral tests. For the optogenetic manipulation, mice were placed in the

center of the apparatus and a 12-min behavioral assay was performed with a 3-min Laser OFF and 3-min Laser ON administration pattern. The open field chamber was cleaned with 75% ethanol between each trial and the moving traces were tracked by ANY-Maze software. Total distance traveled and time spent in the center zone were analyzed.

Elevated plus maze (EPM). The EPM apparatus consisted of a central square (50 mm × 50 mm), two open arms without walls (300mm length) and two closed arms with walls (300mm length, 200mm height). For the optogenetic manipulation, mice were placed in the center of the EPM facing closed arm and a 12-min behavioral assay was performed with a 3-min Laser OFF and 3-min Laser ON administration pattern. Moving traces were tracked by ANY-Maze software. Time spent in the open arm were analyzed.

Real time place preference or aversion (RTPP). A two-chamber apparatus (500 mm × 250 mm) was used for the test. The mice were allowed to move freely in the apparatus for 10 minutes on the first day. The mice with over 80% initial place preference were excluded from the experiment. On the following two days, a 465 nm laser stimulation was delivered when mice entered the laser-coupled side for a 10min real-time laser coupling test. Moving traces were tracked by ANY-Maze software. The percentage of time in the laser-coupling side and the preference index were analyzed.

Food intake analysis. For the food intake test, mice had ad libitum access to chow in the home cage both prior to and following food intake trials. Each mouse was housed individually and its intake of normal and high-fat food was measured separately over a 24-hour period. For the optogenetic manipulation, mice were connected to a 473 nm blue laser and transferred to a transparent cage for 1-hour to habituate to the testing environment. Initially, a 10-min food intake test was conducted without any laser stimulation, followed by a 10 min trial with laser stimulation. For the 10-min trial, a 473-nm blue laser light with a pulse duration of 10-ms and varying frequencies (1Hz, 5Hz, 10Hz and 20 Hz) were applied to zona incerta, after which a 30-minute period without stimulation ensued. For the 4 ×10-

min trial, a 10-min session of light stimulation (10 ms, 20 Hz) was followed by 30 min interval without stimulation, repeated four times[34].

Novel object recognition test. The task was conducted under identical environmental conditions to those of the open-field test, consist of a training phase (also known as the familiarization phase) followed by a testing phase, with a 1-hour interval. During the training phase, mice were exposed to two objects that were identical in terms of shape, color, and odor. These objects were positioned close to the corners of one wall within the testing arena. Each mouse was placed in the center of the arena and given 10 minutes to explore the objects. In the subsequent test phase, one object was a duplicate of the one used in the training phase, while the other was a new object. Each mouse was again placed in the arena and optical stimulation was applied during the test phase, which lasted 5 minutes. The arrangement of objects during the test phase was randomly alternated between the animals within each group. The durations of time spent by the mice exploring both the familiar and the novel objects were measured.

Adult male mice were used for all the behavioral analysis above.

EEG-EMG recordings and analysis

Electroencephalogram (EEG) recordings were made from three screws on top of the left and right cortex, at AP –3.5 mm, ML 2.5 mm and AP +1.0 mm, ML ±1.5 mm, respectively. For electromyogram (EMG) recording, two EMG electrodes (P01965, CALMONT, USA) were inserted into the neck musculature and a reference screw was implanted into the skull above the right cortex. Insulated leads from the EEG and EMG electrodes were soldered to a 2 × 3 pin header, which was secured to the skull by dental cement. For EEG and EMG recordings with fiber photometry recording or optogenetic manipulation, optical fiber was placed in the same surgery for EEG and EMG implants. After surgery, mice were allowed to recover for at least 1week before experiments. Experimental and control animals were subjected to exactly the same surgical and behavioral manipulations. All the implanted mice were housed in a 12-h dark - 12-h light cycle (Lights on between

07:00 (ZT0) and 19:00 (ZT12)). For optogenetic activation of Pde11a positive neurons in ZIm, each trial consisted of a 20 Hz pulse train (10 ms per pulse) lasting for 120 s and inter-trial interval was chosen randomly between 10 or 15 min. For chemogenetic activation or inhibition of Pde11a positive neurons in ZIm, we used the virus-transfected mice with saline as control compared to mice with CNO (1 mg/kg in saline) intraperitoneal injection. The following injection protocol was used for analysis of all mice injected with AAV virus carrying cre-dependent expression of hM3Dq or hM4Di: on day 1, we performed two consecutive saline injections at 12-h intervals at ZT5 (12:00) and ZT17 (24:00) and CNO at the same times on day 2. For DTA-mediated ablation of Pde11a positive neurons in ZIm, we recorded the virus-transfected mice for 24hr. The EEG and EMG signals were recorded and amplified using PowerLab system (AD Instruments, Australia). NREM, REM and wake states were analyzed for each 5-s epoch by LabChart8 (wake: desynchronized EEG and high EMG activity; NREM sleep: synchronized EEG with high power at 0.5–4 Hz and low EMG activity; REM sleep: desynchronized EEG with high power at theta frequencies (6–9 Hz) and low EMG activity. Experimenters were blinded to all training and behavioral assessments. Adult male mice were used for the EEG-EMG recording experiments.

Quantification and statistical analysis

Statistical analysis was performed using Graph-Pad Prism 6, Matlab 2019a. The following statistical tests were used: two-tailed *t*-test and one-way analysis of variance (ANOVA). Data are presented as mean ± SEM. The number of cells, animals or experimental replicates are indicated in the figure legends. The animals were randomly assigned into experimental and control groups. All behavioral experiments and data analyses were conducted blindly.

Data availability

The raw sequence data reported in this paper have been deposited in the Genome Sequence Archive in National Genomics Data Center, China National Center for Bioinformation, Beijing Institute of Genomics, Chinese Academy of Sciences (GSA: CRA017157) that are publicly accessible at https://ngdc.cncb.ac.cn/gsa. Source data are provided with this paper.

References

1. Zeng, H. & Sanes, J.R. Neuronal cell-type classification: challenges, opportunities and the path forward. *Nat Rev Neurosci* **18**, 530-546 (2017).
2. Zeng, H. What is a cell type and how to define it? *Cell* **185**, 2739-2755 (2022).
3. Yao, Z.*, et al.* A taxonomy of transcriptomic cell types across the isocortex and hippocampal formation. *Cell* **184**, 3222-3241 e3226 (2021).
4. Tasic, B.*, et al.* Shared and distinct transcriptomic cell types across neocortical areas. *Nature* **563**, 72-78 (2018).
5. Yao, Z.*, et al.* A high-resolution transcriptomic and spatial atlas of cell types in the whole mouse brain. *Nature* **624**, 317-332 (2023).
6. DeFelipe, J.*, et al.* New insights into the classification and nomenclature of cortical GABAergic interneurons. *Nat Rev Neurosci* **14**, 202-216 (2013).
7. Gouwens, N.W.*, et al.* Classification of electrophysiological and morphological neuron types in the mouse visual cortex. *Nature neuroscience* **22**, 1182-1195 (2019).
8. Gao, L.*, et al.* Single-neuron analysis of dendrites and axons reveals the network organization in mouse prefrontal cortex. *Nat Neurosci* **26**, 1111-1126 (2023).
9. Cadwell, C.R.*, et al.* Electrophysiological, transcriptomic and morphologic profiling of single neurons using Patch-seq. *Nat Biotechnol* **34**, 199-203 (2016).
10. Fuzik, J.*, et al.* Integration of electrophysiological recordings with single-cell RNA-seq data identifies neuronal subtypes. *Nat Biotechnol* **34**, 175-183 (2016).
11. Gouwens, N.W.*, et al.* Integrated Morphoelectric and Transcriptomic Classification of Cortical GABAergic Cells. *Cell* **183**, 935-953 e919 (2020).
12. Scala, F.*, et al.* Phenotypic variation of transcriptomic cell types in mouse motor cortex. *Nature* **598**, 144-150 (2021).
13. Kalmbach, B.E.*, et al.* Signature morpho-electric, transcriptomic, and dendritic properties of human layer 5 neocortical pyramidal neurons. *Neuron* **109**, 2914-2927 e2915 (2021).
14. Zhang, M.*, et al.* Spatially resolved cell atlas of the mouse primary motor cortex by MERFISH. *Nature* **598**, 137-143 (2021).
15. Chen, A.*, et al.* Spatiotemporal transcriptomic atlas of mouse organogenesis using DNA nanoball-patterned arrays. *Cell* **185**, 1777-1792 e1721 (2022).
16. Zhang, M.*, et al.* Molecularly defined and spatially resolved cell atlas of the whole mouse brain. *Nature* **624**, 343-354 (2023).

884 17. Yao, S., *et al.* A whole-brain monosynaptic input connectome to neuron classes
885 in mouse visual cortex. *Nat Neurosci* **26**, 350-364 (2023).
886 18. Zhang, Z., *et al.* Epigenomic diversity of cortical projection neurons in the
887 mouse brain. *Nature* **598**, 167-173 (2021).
888 19. Huang, L., *et al.* BRICseq Bridges Brain-wide Interregional Connectivity to
889 Neural Activity and Gene Expression in Single Animals. *Cell* **183**, 2040 (2020).
890 20. Sun, Y.C., *et al.* Integrating barcoded neuroanatomy with spatial
891 transcriptional profiling enables identification of gene correlates of projections. *Nat*
892 *Neurosci* **24**, 873-885 (2021).
893 21. Caputi, A., Melzer, S., Michael, M. & Monyer, H. The long and short of GABAergic
894 neurons. *Curr Opin Neurobiol* **23**, 179-186 (2013).
895 22. Melzer, S. & Monyer, H. Diversity and function of corticopetal and corticofugal
896 GABAergic projection neurons. *Nat Rev Neurosci* **21**, 499-515 (2020).
897 23. Malik, R., Li, Y., Schamiloglu, S. & Sohal, V.S. Top-down control of hippocampal
898 signal-to-noise by prefrontal long-range inhibition. *Cell* **185**, 1602-1617 e1617
899 (2022).
900 24. Lee, A.T., Vogt, D., Rubenstein, J.L. & Sohal, V.S. A class of GABAergic neurons
901 in the prefrontal cortex sends long-range projections to the nucleus accumbens and
902 elicits acute avoidance behavior. *J Neurosci* **34**, 11519-11525 (2014).
903 25. Melzer, S., *et al.* Long-range-projecting GABAergic neurons modulate
904 inhibition in hippocampus and entorhinal cortex. *Science* **335**, 1506-1510 (2012).
905 26. Szabo, G.G., *et al.* Ripple-selective GABAergic projection cells in the
906 hippocampus. *Neuron* **110**, 1959-1977 e1959 (2022).
907 27. Schroeder, A., *et al.* Inhibitory top-down projections from zona incerta mediate
908 neocortical memory. *Neuron* **111**, 727-738 e728 (2023).
909 28. Saunders, A., *et al.* A direct GABAergic output from the basal ganglia to frontal
910 cortex. *Nature* **521**, 85-89 (2015).
911 29. Schlesiger, M.I., *et al.* Two septal-entorhinal GABAergic projections
912 differentially control coding properties of spatially tuned neurons in the medial
913 entorhinal cortex. *Cell Rep* **34**, 108801 (2021).
914 30. Mitrofanis, J. Some certainty for the "zone of uncertainty"? Exploring the
915 function of the zona incerta. *Neuroscience* **130**, 1-15 (2005).
916 31. Wang, X., Chou, X.L., Zhang, L.I. & Tao, H.W. Zona Incerta: An Integrative Node
917 for Global Behavioral Modulation. *Trends Neurosci* **43**, 82-87 (2020).
918 32. Yang, Y., *et al.* Whole-Brain Connectome of GABAergic Neurons in the Mouse
919 Zona Incerta. *Neurosci Bull* **38**, 1315-1329 (2022).
920 33. Wang, Q., *et al.* The Allen Mouse Brain Common Coordinate Framework: A 3D
921 Reference Atlas. *Cell* **181**, 936-953 e920 (2020).
922 34. Zhang, X. & van den Pol, A.N. Rapid binge-like eating and body weight gain
923 driven by zona incerta GABA neuron activation. *Science* **356**, 853-859 (2017).
924 35. Liu, K., *et al.* Lhx6-positive GABA-releasing neurons of the zona incerta
925 promote sleep. *Nature* **548**, 582-587 (2017).
926 36. Shang, C., *et al.* A subcortical excitatory circuit for sensory-triggered predatory
927 hunting in mice. *Nat Neurosci* **22**, 909-920 (2019).

928 37. Zhao, Z.D., *et al.* Zona incerta GABAergic neurons integrate prey-related
929 sensory signals and induce an appetitive drive to promote hunting. *Nat Neurosci* **22**,
930 921-932 (2019).
931 38. Ogasawara, T., *et al.* A primate temporal cortex-zona incerta pathway for
932 novelty seeking. *Nat Neurosci* **25**, 50-60 (2022).
933 39. Venkataraman, A., *et al.* Modulation of fear generalization by the zona incerta.
934 *Proc Natl Acad Sci U S A* **116**, 9072-9077 (2019).
935 40. Li, Z., Rizzi, G. & Tan, K.R. Zona incerta subpopulations differentially encode
936 and modulate anxiety. *Sci Adv* **7**, eabf6709 (2021).
937 41. Ahmadlou, M., *et al.* A cell type-specific cortico-subcortical brain circuit for
938 investigatory and novelty-seeking behavior. *Science* **372** (2021).
939 42. Lin, S., *et al.* Somatostatin-Positive Neurons in the Rostral Zona Incerta
940 Modulate Innate Fear-Induced Defensive Response in Mice. *Neurosci Bull* (2022).
941 43. Velmeshev, D., *et al.* Single-cell genomics identifies cell type-specific molecular
942 changes in autism. *Science* **364**, 685-689 (2019).
943 44. Huang, K.W., *et al.* Molecular and anatomical organization of the dorsal raphe
944 nucleus. *Elife* **8** (2019).
945 45. Zeisel, A., *et al.* Molecular Architecture of the Mouse Nervous System. *Cell* **174**,
946 999-1014 e1022 (2018).
947 46. La Manno, G., *et al.* Molecular Diversity of Midbrain Development in Mouse,
948 Human, and Stem Cells. *Cell* **167**, 566-580 e519 (2016).
949 47. Kee, N., *et al.* Single-Cell Analysis Reveals a Close Relationship between
950 Differentiating Dopamine and Subthalamic Nucleus Neuronal Lineages. *Cell Stem Cell*
951 **20**, 29-40 (2017).
952 48. Chen, R., Wu, X., Jiang, L. & Zhang, Y. Single-Cell RNA-Seq Reveals Hypothalamic
953 Cell Diversity. *Cell Rep* **18**, 3227-3241 (2017).
954 49. Zhang, Y.H., *et al.* Cascade diversification directs generation of neuronal
955 diversity in the hypothalamus. *Cell Stem Cell* **28**, 1483-1499 e1488 (2021).
956 50. Marques, S., *et al.* Oligodendrocyte heterogeneity in the mouse juvenile and
957 adult central nervous system. *Science* **352**, 1326-1329 (2016).
958 51. Lein, E.S., *et al.* Genome-wide atlas of gene expression in the adult mouse brain.
959 *Nature* **445**, 168-176 (2007).
960 52. Xu, Y., *et al.* Identification of a neurocircuit underlying regulation of feeding by
961 stress-related emotional responses. *Nat Commun* **10**, 3446 (2019).
962 53. Mu, M.D., *et al.* A limbic circuitry involved in emotional stress-induced
963 grooming. *Nat Commun* **11**, 2261 (2020).
964 54. Gao, Z.R., *et al.* Tac1-Expressing Neurons in the Periaqueductal Gray Facilitate
965 the Itch-Scratching Cycle via Descending Regulation. *Neuron* **101**, 45-59 e49 (2019).
966 55. Xie, Z., *et al.* A brain-to-spinal sensorimotor loop for repetitive self-grooming.
967 *Neuron* **110**, 874-890 e877 (2022).
968 56. Zhang, Y.F., *et al.* Ventral striatal islands of Calleja neurons control grooming
969 in mice. *Nat Neurosci* **24**, 1699-1710 (2021).
970 57. Kalueff, A.V., *et al.* Neurobiology of rodent self-grooming and its value for
971 translational neuroscience. *Nat Rev Neurosci* **17**, 45-59 (2016).

58. Sun, J., *et al.* Excitatory SST neurons in the medial paralemniscal nucleus control repetitive self-grooming and encode reward. *Neuron* **110**, 3356-3373 e3358 (2022).
59. Mangieri, L.R., *et al.* A neural basis for antagonistic control of feeding and compulsive behaviors. *Nat Commun* **9**, 52 (2018).
60. Liu, Q., *et al.* An iterative neural processing sequence orchestrates feeding. *Neuron* **111**, 1651-1665 e1655 (2023).
61. Ahnaou, A., *et al.* Long-term enhancement of REM sleep by the pituitary adenylyl cyclase-activating polypeptide (PACAP) in the pontine reticular formation of the rat. *Eur J Neurosci* **11**, 4051-4058 (1999).
62. Maloney, K.J., Mainville, L. & Jones, B.E. c-Fos expression in GABAergic, serotonergic, and other neurons of the pontomedullary reticular formation and raphe after paradoxical sleep deprivation and recovery. *J Neurosci* **20**, 4669-4679 (2000).
63. Yamahachi, H., Marik, S.A., McManus, J.N., Denk, W. & Gilbert, C.D. Rapid axonal sprouting and pruning accompany functional reorganization in primary visual cortex. *Neuron* **64**, 719-729 (2009).
64. Bagri, A., Cheng, H.J., Yaron, A., Pleasure, S.J. & Tessier-Lavigne, M. Stereotyped pruning of long hippocampal axon branches triggered by retraction inducers of the semaphorin family. *Cell* **113**, 285-299 (2003).
65. Luo, L. & O'Leary, D.D. Axon retraction and degeneration in development and disease. *Annu Rev Neurosci* **28**, 127-156 (2005).
66. Wen, S., *et al.* Spatiotemporal single-cell analysis of gene expression in the mouse suprachiasmatic nucleus. *Nat Neurosci* **23**, 456-467 (2020).
67. Kim, D.W., *et al.* Gene regulatory networks controlling differentiation, survival, and diversification of hypothalamic Lhx6-expressing GABAergic neurons. *Commun Biol* **4**, 95 (2021).
68. Puelles, L., *et al.* LacZ-reporter mapping of Dlx5/6 expression and genoarchitectural analysis of the postnatal mouse prethalamus. *J Comp Neurol* **529**, 367-420 (2021).
69. Wang, X.Y., *et al.* A cross-modality enhancement of defensive flight via parvalbumin neurons in zonal incerta. *Elife* **8** (2019).
70. Kalueff, A.V. & Tuohimaa, P. Grooming analysis algorithm for neurobehavioural stress research. *Brain Res Brain Res Protoc* **13**, 151-158 (2004).
71. Kulkosky, P.J., Gibbs, J. & Smith, G.P. Feeding suppression and grooming repeatedly elicited by intraventricular bombesin. *Brain Res* **242**, 194-196 (1982).
72. Krahn, D.D., Gosnell, B.A., Grace, M. & Levine, A.S. CRF antagonist partially reverses CRF- and stress-induced effects on feeding. *Brain Res Bull* **17**, 285-289 (1986).
73. Rodrigo-Angulo, M.L., Heredero, S., Rodriguez-Veiga, E. & Reinoso-Suarez, F. GABAergic and non-GABAergic thalamic, hypothalamic and basal forebrain projections to the ventral oral pontine reticular nucleus: their implication in REM sleep modulation. *Brain Res* **1210**, 116-125 (2008).
74. Vanini, G., Wathen, B.L., Lydic, R. & Baghdoyan, H.A. Endogenous GABA levels in the pontine reticular formation are greater during wakefulness than during rapid eye movement sleep. *J Neurosci* **31**, 2649-2656 (2011).

1017 75. Xi, M.C., Morales, F.R. & Chase, M.H. Evidence that wakefulness and REM sleep
1018 are controlled by a GABAergic pontine mechanism. *J Neurophysiol* **82**, 2015-2019
1019 (1999).
1020 76. Camacho-Arroyo, I., Alvarado, R., Manjarrez, J. & Tapia, R. Microinjections of
1021 muscimol and bicuculline into the pontine reticular formation modify the sleep-
1022 waking cycle in the rat. *Neurosci Lett* **129**, 95-97 (1991).
1023 77. Blanco-Centurion, C., Vidal-Ortiz, A., Sato, T. & Shiromani, P.J. Activity of GABA
1024 neurons in the zona incerta and ventral lateral periaqueductal grey is biased towards
1025 sleep. *Sleep* **46** (2023).
1026 78. Chen, K.S.*, et al.* A Hypothalamic Switch for REM and Non-REM Sleep. *Neuron*
1027 **97**, 1168-1176 e1164 (2018).
1028 79. Weber, F.*, et al.* Control of REM sleep by ventral medulla GABAergic neurons.
1029 *Nature* **526**, 435-438 (2015).
1030 80. Xu, M.*, et al.* Basal forebrain circuit for sleep-wake control. *Nat Neurosci* **18**,
1031 1641-1647 (2015).
1032 81. Pinto, L.*, et al.* Fast modulation of visual perception by basal forebrain
1033 cholinergic neurons. *Nat Neurosci* **16**, 1857-1863 (2013).
1034 82. Liu, D. & Dan, Y. A Motor Theory of Sleep-Wake Control: Arousal-Action Circuit.
1035 *Annu Rev Neurosci* **42**, 27-46 (2019).
1036 83. McGinley, M.J.*, et al.* Waking State: Rapid Variations Modulate Neural and
1037 Behavioral Responses. *Neuron* **87**, 1143-1161 (2015).
1038 84. John, J., Wu, M.F., Boehmer, L.N. & Siegel, J.M. Cataplexy-active neurons in the
1039 hypothalamus: implications for the role of histamine in sleep and waking behavior.
1040 *Neuron* **42**, 619-634 (2004).
1041 85. Plaha, P., Ben-Shlomo, Y., Patel, N.K. & Gill, S.S. Stimulation of the caudal zona
1042 incerta is superior to stimulation of the subthalamic nucleus in improving
1043 contralateral parkinsonism. *Brain* **129**, 1732-1747 (2006).
1044 86. Mostofi, A.*, et al.* Outcomes from deep brain stimulation targeting subthalamic
1045 nucleus and caudal zona incerta for Parkinson's disease. *NPJ Parkinsons Dis* **5**, 17
1046 (2019).
1047 87. Summa, K.C.*, et al.* Disrupted sleep-wake regulation in the MCI-Park mouse
1048 model of Parkinson's disease. *NPJ Parkinsons Dis* **10**, 54 (2024).
1049 88. Tandberg, E., Larsen, J.P. & Karlsen, K. A community-based study of sleep
1050 disorders in patients with Parkinson's disease. *Mov Disord* **13**, 895-899 (1998).
1051 89. Corces, M.R.*, et al.* An improved ATAC-seq protocol reduces background and
1052 enables interrogation of frozen tissues. *Nat Methods* **14**, 959-962 (2017).
1053 90. Tuesta, L.M.*, et al.* In vivo nuclear capture and molecular profiling identifies
1054 Gmeb1 as a transcriptional regulator essential for dopamine neuron function. *Nat*
1055 *Commun* **10**, 2508 (2019).

1056

Acknowledgement

We thank Research Assistant Zhaoxiaonan Lin from the Core Facilities of Zhejiang University School of Medicine and Dr. Sanhua Fang from the Core Facilities of Zhejiang University Institute of Neuroscience for technical support. We thank Drs. Shumin Duan, Jianhong Luo, Ying Shen (Zhejiang University) for suggestions on the project. This work was supported by grants from the Ministry of Science and Technology (2019YFA0110103 to J.C.), National Natural Science Foundation of China (81870898 to J.C.; 82090030 and 82288101 to X.-M.L.), Zhejiang Provincial Natural Science Foundation (LR18H090002), STI2030-Major Projects (2021ZD0202700 to X.-M.L.; 2021ZD0203400 to Y.-Q.Y.), Key-Area Research and Development Program of Guangdong Province (2019B030335001 to X.-M.L.), Key R&D Program of Zhejiang Province (2020C03009 and 2021C03001 to X.-M.L.), Fundamental Research Funds for the Central Universities (2021FZZX001-37 to X.-M.L.), CAMS Innovation Fund for Medical Sciences (2019-I2M-5-057 to X.-M.L.), Innovative and Entrepreneur Team of Zhejiang for 2020 Biomarker-Driven Basic and Translational Research on Major Brain Diseases (2020R01001 to X.-M.L.), National Natural Science Foundation of China Major Project (T2293733 to Y.-Q.Y.), Postdoctoral Fellowship Program of CPSF (GZC20232285 to M.Z.), and the Non-profit Central Research Institute Fund of Chinese Academy of Medical Sciences (2023-PT310-01).

Author Contributions

J.C. conceived and designed the project, M.Z. M.W. S.L. performed in vivo circuit tracing, optogenetics, behavioral experiments and data analysis. M.Z. M.W. performed immunohistochemistry staining, fluorescence in situ hybridization and confocal imaging, J.P. H.Z. Y.Z. L.S. performed single-nuclei RNA sequencing and data analysis. X.D. performed electrophysiology experiments and data analysis. M.Z. M.W. H.Z. Y.Y. performed EEG/EMG recordings and data analysis. J.C. X.L.

analyzed data and supervised the project. J.C. prepared the manuscript with inputs from all authors.

Competing Interest

All authors claim that there are no competing interests.

Figure legends

Fig. 1: Single-nucleus transcriptomic sequencing reveals major cell type composition in zona incerta.

a, Schematic diagram showing the workflow for microdissection of zona incerta from brain slices in green fluorescent protein knock-in transporter line Gad67-GFP mice, single nucleus isolation and RNA sequencing by 10x Genomics. UMAP plot of the processed dataset containing 15,375 single nuclei collected from two independent cohorts of 10x Genomics experiments (n = 6 mice for each cohort). The cell clusters were annotated according to canonical cell type-specific marker genes.

b, UMAP plot showing re-clustering the excitatory and inhibitory neurons into ten glutamatergic neuron clusters (Glu_N1 to Glu_N10) and twelve GABAergic neuron clusters (GABA_N1 to GABA_N12).

c, Heatmap showing the differentially expressed genes (DEGs) among neuron clusters from snRNA-seq dataset. The regional identity (top) of the neuron clusters were annotated by the expression of region specific DEGs (right). TH, Thalamus; STN, Subthalamus nucleus; PVN, Paraventricular nucleus; Hypo, Hypothalamus; ZI, Zona incerta; PIL, Posterior intralaminar thalamus nucleus; TRN, Thalamic reticular nucleus; UnA, Un-Annotated region.

d, UMAP plot showing the GABAergic neuron clusters (GABA_N4 to GABA_N9) associated with zona incerta.

e, Dotplot showed the differential expressed genes (DEGs) of GABAergic neuron clusters associated with zona incerta. Source data are provided as a Source Data file.

Fig. 2: Region-specific genes expression of GABAergic neuron subtypes in subregions of zona incerta.

a, Violin Plots showed the expression level of selected DEG genes of GABAergic neuron clusters in zona incerta.

b, Representative images (**b**) and statistical results (**c**) showing the density of *Ecel1* (ZIr *vs* ZIm, ****P < 0.0001; ZIr *vs* ZIc, ****P < 0.0001; ZIm *vs* ZIc, *P = 0.0443), *Cdh23* (ZIr *vs* ZIm, **P =0.0075; ZIr *vs* ZIc, **P =0.0039), *Pax6* (ZIr *vs* ZIm, ***P =0.0004; ZIr *vs* ZIc, ***P =0.0007), *Pde11a* (ZIr *vs* ZIm, **P =0.0038; ZIm *vs* ZIc, ***P =0.0006), *Ptprk* (ZIr *vs* ZIm, **P =0.0020; ZIr *vs* ZIc, *P =0.0119), *Nos1* (ZIr *vs* ZIm, **P =0.0062; ZIr *vs* ZIc, **P =0.0092) in the ZIr, ZIm and ZIc, n = 9 brain slices from 3 mice per group. Scale bar, 200 μm. One-way ANOVA and tukey's multiple comparisons test.

d, Representative images (**d**) and statistical results (**e**) showing the overlap between *Ecel1*, *Pde11a* and *Ptprk* in different brain sections of ZIr, ZIm and ZIc. The cell numbers in ZIr (*Ecel1*$^+$: 410.0 ± 9.539 cells; *Ecel1*$^+$*Pde11a*$^+$: 9.33 ± 1.20 cells; *Ecel1*$^+$*Ptprk*$^+$: 43.33 ± 5.49 cells; *Pde11a*$^+$*Ptprk*$^+$: 4.33 ± 0.88 cells; *Ecel1*$^+$*Pde11a*$^+$*Ptprk*$^+$: 1.67 ± 0.33 cells), ZIm (*Pde11a*$^+$: 361.0 ± 23.81 cells; *Ecel1*$^+$*Pde11a*$^+$: 1.67 ± 0.67 cells; *Ecel1*$^+$*Ptprk*$^+$: 4.67 ± 0.88 cells; *Pde11a*$^+$*Ptprk*$^+$: 2.67 ± 0.33 cells; *Ecel1*$^+$*Pde11a*$^+$*Ptprk*$^+$: 0 ± 0 cells) and ZIc (*Ptprk*$^+$: 132.3 ± 16.13 cells; *Ecel1*$^+$*Pde11a*$^+$: 3.33 ± 0.33 cells; *Ecel1*$^+$*Ptprk*$^+$: 7.33 ± 0.88 cells; *Pde11a*$^+$*Ptprk*$^+$: 2.00 ± 0.58 cells; *Ecel1*$^+$*Pde11a*$^+$*Ptprk*$^+$: 2.33 ± 0.88 cells) were shown respectively. N = 9 brain slices from 3 mice per group. Scale bars, 100 μm and 20 μm (zoom-in image). Data are presented as mean ± SEM. Source data are provided as a Source Data file.

Fig. 3: Generation and validation of transgenic mice Ecel1-Cre and Pde11a-Cre.

a, Representative images showing the expression of *Ecel1* (**a**) and *Pde11a* (**b**) in *Slc32a1* (Vgat) positive neurons in ZIr or ZIm. Scale bar, 50μm.

c, The percentage of *Ecel1*$^+$*Slc32a1*$^+$ cells relative to all *Ecel1*$^+$ or *Slc32a1*$^+$ cells in ZIr (*Ecel1*$^+$*Slc32a1*$^+$/*Ecel1*$^+$, 96.39±1.19%; *Ecel1*$^+$*Slc32a1*$^+$/*Slc32a1*$^+$, 59.69±6.28%) and the percentage of *Pde11a*$^+$*Slc32a1*$^+$ cells relative to all *Pde11a*$^+$ or *Slc32a1*$^+$ cells in ZIm (*Pde11a*$^+$*Slc32a1*$^+$/*Pde11a*$^+$, 97.7±2.3%; *Pde11a*$^+$*Slc32a1*$^+$/*Slc32a1*$^+$, 33.92±9.67%). n=9 brain slices from 3 mice per group.

d, Schematic diagram showing the generation of Ecel1-Cre or Pde11a-Cre knock-in mice.

e, Representative images showing the Cre and *Ecel1* or the Cre and *Pde11a* expression in ZIr, ZIm and ZIc. Scale bars, 100μm and 20μm (zoom-in image).

f, The percentage of *Ecel1*$^+$Cre$^+$ relative to all Cre$^+$ or *Ecel1*$^+$ neurons in ZIr (*Ecel1*$^+$Cre$^+$/Cre$^+$,93.87±1.45%; *Ecel1*$^+$Cre$^+$/*Ecel1*$^+$, 96.41±0.92%), ZIm (*Ecel1*$^+$Cre$^+$/Cre$^+$, 91.11±2.81%; *Ecel1*$^+$Cre$^+$/*Ecel1*$^+$, 86.46±4.39%) and ZIc (*Ecel1*$^+$Cre$^+$/Cre$^+$, 78.41±4.75%; *Ecel1*$^+$Cre$^+$/*Ecel1*$^+$, 78.00±5.95%) of Ecel1-Cre mice. n = 9 brain slices from 3 mice per group.

g, Statistical results showing the expression and distribution of Cre in the ZIr (71.95±1.12%), ZIm (12.76±0.67%) and ZIc (15.28±0.49%) of Ecel1-Cre mice. ZIr *vs* ZIm, ****P<0.0001; ZIr *vs* ZIc, ****P<0.0001. N = 9 brain slices from 3 mice per group.

h, The percentage of *Pde11a*$^+$Cre$^+$ relative to all Cre+ or *Pde11a*$^+$ neurons in ZIr (*Pde11a*$^+$Cre$^+$/Cre$^+$, 97.70±2.30%; *Pde11a*$^+$Cre$^+$/*Pde11a*$^+$, 99.48±0.52%), ZIm (*Pde11a*$^+$Cre$^+$/Cre$^+$, 99.70±0.15%; *Pde11a*$^+$Cre$^+$/*Pde11a*$^+$, 98.91±0.22%) and ZIc (*Pde11a*$^+$Cre$^+$/Cre$^+$, 93.00±4.72%; *Pde11a*$^+$Cre$^+$/*Pde11a*$^+$, 89.73±3.06%) of Pde11a-Cre mice. n=9 brain slices from 3 mice per group.

i, Statistical results showing the expression and distribution of Cre in the ZIr (4.43±2.54%), ZIm (90.33±2.91%) and ZIc (5.24±1.27%) of Pde11a-Cre mice. ZIr *vs* ZIm, ****P<0.0001; ZIm *vs* ZIc, ****P< 0.0001. N=9 brain slices from 3 mice per group.

One-way ANOVA and tukey's multiple comparisons test for (**g**) and (**i**). Data are presented as mean±SEM. Source data are provided as a Source Data file.

Fig. 4: Distinct efferent projections of Ecel1 positive neurons in the rostral ZI and Pde11a positive neurons in the medial ZI.

a, Schematic diagram and representative images showing the stereotaxic unilateral injection of Cre-dependent AAV mediated mGFP and synaptophysin-mRuby to specifically label Ecel1 positive neurons in the rostral ZI (ZIr^{Ecel1}) of Ecel1-Cre mice (**a**) or Pde11a positive neurons in the medial ZI (ZIm^{Pde11a}) of Pde11a-Cre mice (**b**). Scale bar, 250 μm. The experiment was independently repeated 3 times with similar results for each mouse strain.

c, Representative images showing dense distribution of mGFP and mRuby positive axons from the ZIr^{Ecel1} neurons to the PAG and from ZIm^{Pde11a} neuron to the PRF. Scale bar, 100 μm.

d, Quantification of integrated fluorescence intensity of mRuby and mGFP-labeled axon terminals in PAG or PRF of ZIr^{Ecel1} and ZIm^{Pde11a} neurons. *P = 0.015, **P = 0.0032, n = 3 mice.

e, Quantification of relative fluorescent density of mRuby and mGFP-labeled axon terminals of ZIr^{Ecel1} and ZIm^{Pde11a} neurons in the target brain regions. N = 9 slices from 3 mice for each brain region. Abbreviations: LS, lateral septal nucleus; POA, preoptic area; PVT, paraventricular thalamic nucleus; Re, reuniens thalamic nucleus; LH, lateral hypothalamic area; MD, mediodorsal thalamic nucleus; Po, posterior thalamic nucleus; Auv, secondary auditory cortex; APTD, anterior pretectal nucleus; Dk, nucleus of Darkschewitsch; RN, red nucleus; PAG,

periaqueductal gray; PRF, pontine reticular nucleus, oral part; SC, superior colliculus.

Two-tailed unpaired t test for (**d**). Data are presented as mean ± SEM. Source data are provided as a Source Data file.

Fig. 5: Optogenetic activation of ZIr^{Ecel1} neurons and the ZIr^{Ecel1} to PAG pathway both induce self-grooming.

a, Schematic diagram showing optogenetic stimulation of the ChR2-EYFP or EGFP expressing ZIr^{Ecel1} neurons in Ecel1-Cre mice.

b, Schematic diagram showing the behavioral paradigm for measurement of self-grooming behavior upon optogenetic stimulation.

c, Statistic analysis of time spent for self-grooming (left) and grooming bouts (right) in 3 min before, during and after optogenetic stimulation of ZIr^{Ecel1} neurons in ChR2-group (**c**) and EGFP-group (**d**), respectively. Data are presented as mean ± SEM. $^{**}P = 0.0014$, $^{****}P < 0.0001$. Blue column indicates laser stimulation period (5 Hz, 3 min).

e, Schematic diagram showing the recording of inhibitory postsynaptic currents (IPSCs) from PAG neurons evoked by optogenetic stimulation of ChR2-EYFP expressing axon terminals from the ZIr^{Ecel1} to the PAG in acute brain slices.

f, Representative traces and statistical analysis of light-evoked IPSCs recorded in PAG neuron in ACSF and following sequential application of TTX (**f,** 1 μM. $^{**}P = 0.0082$), TTX + 4-AP (**f,** 100 μM. $^{****}P < 0.0001$), or bicuculline (**g,** 20 μM. $^{**}P = 0.0039$). N = 9 neurons from 5 mice, two-tailed paired *t* test. Blue bar indicates optogenetic stimulation (10 ms).

h, Schematic diagram and representative images showing optogenetic stimulation of the ChR2-EYFP or EGFP expressing terminals from ZIr^{Ecel1} to PAG pathway in Ecel1-Cre mice. Scale bar, 100 μm.

i, Statistic analysis showing time spent for self-grooming (left) and grooming bouts (right) in 3 min before, during or after optogenetic stimulation of ZIr^{Ecel1} to PAG pathway in ChR2-group (**i**) and EGFP-group (**j**), respectively. ***P* = 0.0013, ****P* < 0.0001. Blue column indicates laser stimulation period (20 Hz, 3min).

One-way ANOVA for (**c**), (**d**), (**i**) and (**j**). Two-tailed paired *t* test for (**f**) and (**g**). Data are presented as mean ± SEM. Source data are provided as a Source Data file.

Fig. 6: Calcium response patterns of Ecel1 positive neurons in the rostral ZI in self-grooming behavior.

a, Schematic (left) and representative images showing GCamP6s and mCherry expression in ZIr of Ecel1-Cre mice (right). Scale bars, 500 μm and 250 μm (zoom-in image). The experiment was independently repeated 5 times with similar results.

b, Schematic diagram showing the behavioral paradigm for fiber photometry recording in freely moving mice.

c, Schematic diagram (**c**) and statistic analysis (**d**) showing water spray toward the face effectively induced self-grooming behaviors. ***P* = 0.0013, n = 5 mice.

e, Heatmap (**e**) and average calcium transients (**f**) of ZIr^{Ecel1} neurons before, during and after water-spray induced self-grooming. Red trace: recording of GCaMP6s fluorescent signal; Gray trace: recording of control mCherry fluorescent signal. The dashed lines indicate the start or the end of self-grooming. Shaded areas around means indicate standard error of mean (SEM).

g, Statistic analysis showing area under curve (AUC) of average calcium transients of GCamP6s channel compared with mCherry control channel before grooming starts (**P* = 0.0156) and after grooming starts (**P* = 0.0152), before grooming ends (**P* = 0.0385) and after grooming ends (**P* = 0.0114) in water-spray induced self-grooming. N = 5 mice per group.

Two-tailed paired *t*-test for (**d**) and (**g**). Data are presented as mean ± SEM. Source data are provided as a Source Data file.

Fig. 7: Ecel1 positive neurons in the rostral ZI are required for water spray induced self-grooming.

a, Schematic diagram and representative images showing the stereotaxic bilateral injection of AAV-DIO-hM3Dq-mCherry or AAV-DIO-mCherry in the ZIr of Ecel1-Cre mice. Scale bar, 100 μm. The experiment was independently repeated 5 times with similar results.

b-d, Statistic analysis of time spent for self-grooming (**b**), grooming bouts (**c**) and grooming duration per bout (**d**) in 20min following injection of CNO in hM3Dq-group mice compared with mCherry-group mice. $^{**}P = 0.0097$, $^{*}P = 0.0336$.

e, Schematic diagram and representative images showing the injection of AAV-DIO-hM4Di-mCherry to chemogenetically inhibit ZIr^{Ecel1} neurons of Ecel1-Cre mice. Scale bar, 100 μm. The experiment was independently repeated 7 times with similar results.

f, The behavioral paradigm for measurement of water-spray induced self-grooming behavior following injection of CNO in hM4Di-group or mCherry-group mice.

g-i, Statistic analysis of time spent for water-spray induced self-grooming (**g**), grooming bouts (**h**) and grooming duration per bout (**i**) in 20 min following injection of CNO in hM4Di mice. $^{*}P = 0.0117$, $^{**}P = 0.0018$.

j, Schematic diagram showing the stereotaxic bilateral injection of AAV-DIO-DTA to ablate the ZIr^{Ecel1} neurons of Ecel1-Cre mice.

k-m, Statistic analysis of water-spray induced self-grooming time (**k**), grooming bouts (**l**) and grooming duration per bout (**m**) in 20 min following water spray in DTA-group mice. $^{****}P < 0.0001$, $^{**}P = 0.0036$.

Two-tailed unpaired *t*-test for (**b-d**), (**g-i**) and (**k-m**). Data are presented as mean ± SEM. Source data are provided as a Source Data file.

Fig. 8: Calcium response patterns of Pde11a positive neurons in the medial ZI during sleep-wakefulness cycle.

a, Schematic and representative images (right) showing *in vivo* recording of calcium response pattern of GCamP6s- or mCherry-expressing Pde11a positive neurons in ZIm. Gray column indicates the position of optical fiber. Scale bars, 500 μm and 250 μm (zoom-in image). The experiment was independently repeated 5 times with similar results.

b, Schematic diagram showing the behavioral paradigm for fiber photometry, electroencephalogram (EEG) and electromyographic (EMG) recordings in freely moving mice.

c, Sample trace showing the changes of fluorescent calcium signal of ZIm^{Pde11a} neurons aligned to sleep- wakefulness state transitions. NREM (yellow bar), non-rapid eye movement; REM (green bar), rapid eye movement; Wake (blue bar).

d, Average trace and heatmap showing changes of the fluorescent calcium signal of ZIm^{Pde11a} neurons during sleep-wakefulness state transitions. The red trace showed average fluorescent GCaMP6s or control mCherry (gray) signals, while shaded areas indicate standard error of mean (SEM).

e, Statistical analysis of the area under curve (AUC) of average fluorescent calcium signal of ZIm^{Pde11a} neurons during sleep-wakefulness state transitions. N = 5 mice per group. $^*P = 0.0207$ (NREM to REM), $^*P = 0.0332$ (REM to Wake), $^*P = 0.0171$ (Wake to NREM), two-tailed paired *t*-test. Data are presented as mean ± SEM. Source data are provided as a Source Data file.

Fig. 9: Optogenetic activation of ZIm^{Pde11a} neurons promotes wakefulness through the ZIm^{Pde11a} to PRF pathway.

a, Optogenetic stimulation of ChR2-EYFP or EGFP expressing ZIm^{Pde11a} neurons and the behavioral paradigm for EEG-EMG recordings of freely moving Pde11a-Cre mice (**b**).

c, Sample EEG power spectrum, EMG traces and brain states (color coded) during optogenetic activation of ZIm^{Pde11a} neurons. Dark blue: wake; Yellow: NREM; Green: REM. Freq: frequency.

d, The percentage of wake, NREM, or REM states before, during, and after optogenetic stimulation of ZIm^{Pde11a} neurons in ChR2-group (left, n = 5 mice) and EGFP-group (right, n = 6 mice). Shaded areas around means indicate standard error of mean (SEM).

e, Probability change of each state 120s before and during optogenetic stimulation of ZIm^{Pde11a} neurons in ChR2-group compared with EGFP-group. ****$P < 0.0001$, **$P = 0.0021$.

f-h, Schematic diagram (**f**) and representative traces (**g** and **h**, left) showing the recording of evoked IPSCs in PRF neurons in acute brain slices. TTX, *$P = 0.0146$; TTX+4-AP, *$P = 0.0129$ (n = 6 neurons from 4 mice); Bicuculline, *$P = 0.0215$ (n = 7 neurons from 4 mice). Blue bar indicates laser stimulation period (10ms).

i, Optogenetic stimulation of ChR2-EYFP or EGFP expressing terminals of ZIm^{Pde11a} to PRF pathway together with EEG-EMG recordings in Pde11a-Cre mice. Scale bar, 100μm. The experiment was independently repeated 5 times with similar results.

j, Sample EEG power spectrum, EMG traces and brain states during optogenetic activation of ZIm^{Pde11a} to PRF pathway.

k, The percentage of wake, NREM, or REM states before, during, and after optogenetic stimulation of ZIm^{Pde11a} to PRF pathway in ChR2-group (left, n = 5

mice) and EGFP-group (right, n = 5 mice). Shaded areas around means indicate standard error of mean (SEM).

l, Probability change of each state 120s before and during optogenetic stimulation of ZIm^{Pde11a} to PRF pathway in ChR2-group compared with EGFP-group. ****P < 0.0001.

Two-tailed unpaired t test for (**e**) and (**l**). Two-tailed paired t test for (**g**) and (**h**). Data are presented as mean±SEM. Blue bar indicates laser stimulation period (20Hz, 120s). Source data are provided as a Source Data file.

Fig. 10: Selective chemogenetic activation or ablation of ZIm^{Pde11a} neurons bidirectionally regulate sleep-wakefulness cycle.

a, Schematic diagram and representative images showing the injection of AAV-DIO-hM3Dq-mCherry or AAV-DIO-mCherry into the ZIm of Pde11a-Cre mice. Scale bar, 250μm. The experiment was independently repeated 10 times with similar results.

b, Schematic showing sleep recording conditions with saline- or CNO-injection in hM3Dq-group mice.

c-e, The percentage of time spent in wake (**c,** ZT7, ***P=0.0008), NREM sleep (**d**, ZT7, ***P=0.0007) and REM sleep (**e**, ZT7, *P=0.0117) in 2-h bins following injection of saline or CNO in hM3Dq-group mice. Wake, **P=0.0056 (**c**); NREM, **P=0.0080 (**d**); REM, **P=0.009 (**e**).

f-h, Time spent in wake (**f**), NREM sleep (**g**) and REM sleep (**h**) across the 24-hour sleep-wake cycle in hM3Dq-group mice. Wake, **P=0.0083 (**f**); NREM, *P=0.0180 (**g**); REM, *P=0.0304 (**h**).

i, Number and duration (**j**) of wake, NREM sleep and REM sleep episodes during the light phase. Number: Wake, **P=0.0027; NREM, **P=0.0026. Duration: NREM, ****P<0.0001.

k, Schematic diagram showing the injection of AAV-DIO-DTA to ablate the ZIm^{Pde11a} neurons.

l-n, The percentage of time spent in wake (**l**, ZT21, *P=0.0165), NREM sleep (**m**, ZT21, *P=0.0244) and REM sleep (**n**, ZT21, *P=0.0427) in 2-h bins in DTA-group mice compared with mCherry-group mice. REM, **P=0.0040 (**n**).

o-q, Time spent in wake (**o**), NREM sleep (**p**) and REM sleep (**q**) across the 24-hour sleep-wake cycle in DTA-group mice compared with mCherry-group mice. Wake, **P=0.0045 (**o**); NREM, **P=0.0082 (**p**); REM, **P=0.0013 (**q**).

r, Number and duration (**s**) of wake, NREM sleep and REM sleep episodes during the dark phase. Number: Wake, ***P=0.0004; NREM, ***P=0.0005; REM, **P=0.0016. Duration: Wake, ***P=0.0004.

Two-way ANOVA and Sidak's multiple comparisons test for (**c-e**) and (**l-n**). Two-tailed paired t test for (**c-j**). Two-tailed unpaired t test for (**o-s**). Data are presented as mean±SEM. Grey bar indicates the dark phase (ZT12-ZT0). Source data are provided as a Source Data file.

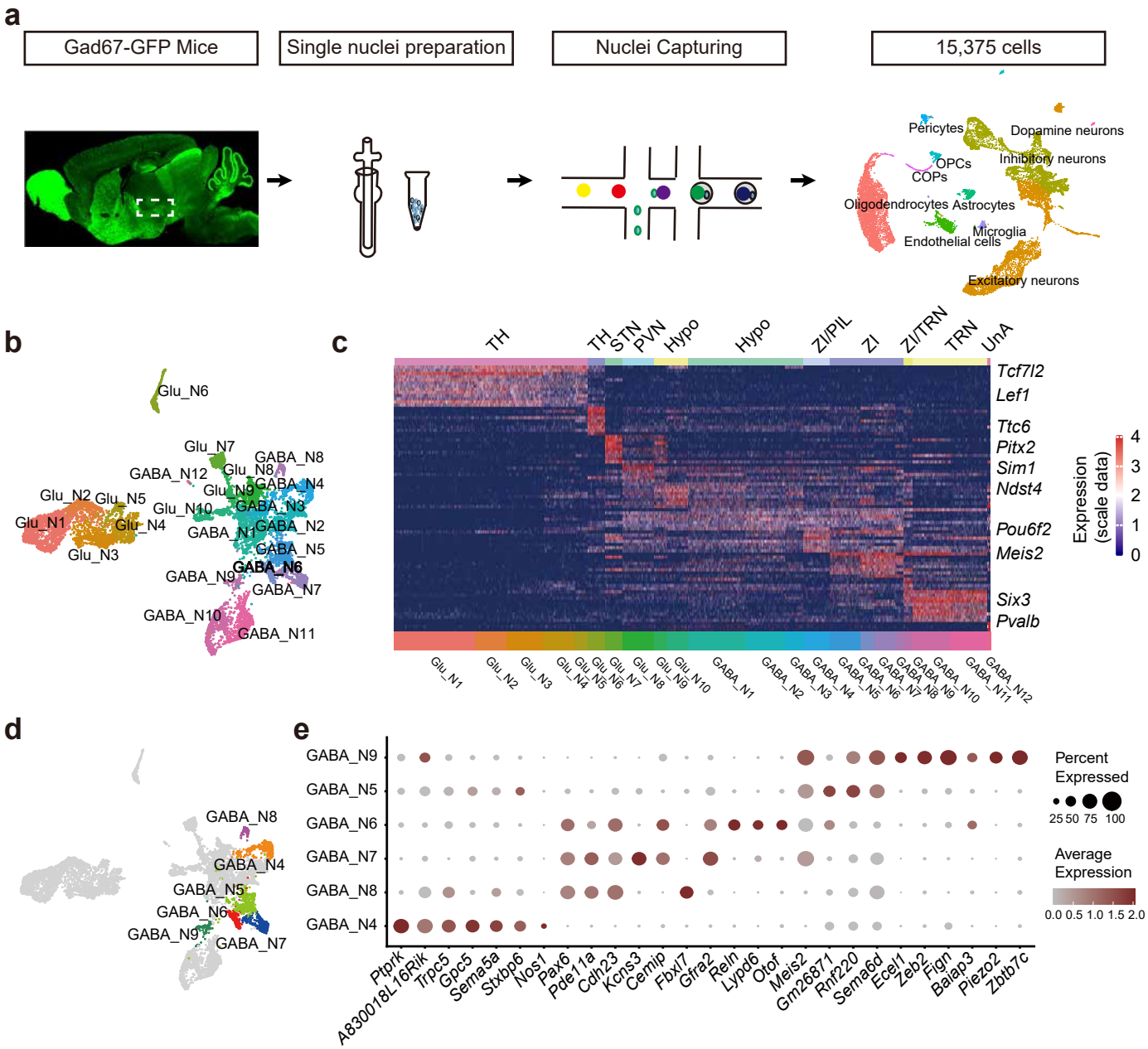
a
Gad67-GFP Mice
Single nuclei preparation
Nuclei Capturing
15,375 cells
Pericytes
Dopamine neurons
OPCs
COPs
Inhibitory neurons
Oligodendrocytes
Astrocytes
Microglia
Endothelial cells
Excitatory neurons
b
Glu_N6
Glu_N7
GABA_N8
GABA_N12
Glu_N8
GABA_N4
Glu_N9
Glu_N2
Glu_N5
Glu_N10
GABA_N3
Glu_N1
Glu_N4
GABA_N1
GABA_N2
Glu_N3
GABA_N5
GABA_N6
GABA_N9
GABA_N7
GABA_N10
GABA_N11
c
TH
TH
STN
PVN
Hypo
Hypo
ZI/PIL
ZI
ZI/TRN
TRN
UnA
Tcf7l2
Lef1
Ttc6
Pitx2
Sim1
Ndst4
Pou6f2
Meis2
Six3
Pvalb
Expression (scale data)
4
3
2
1
0
Glu_N1
Glu_N2
Glu_N3
Glu_N4
Glu_N5
Glu_N6
Glu_N7
Glu_N8
Glu_N9
Glu_N10
GABA_N1
GABA_N2
GABA_N3
GABA_N4
GABA_N5
GABA_N6
GABA_N7
GABA_N8
GABA_N9
GABA_N10
GABA_N11
GABA_N12
d
GABA_N8
GABA_N4
GABA_N5
GABA_N6
GABA_N9
GABA_N7
e
GABA_N9
GABA_N5
GABA_N6
GABA_N7
GABA_N8
GABA_N4
Ptprk
A830018L16Rik
Trpc5
Gpc5
Sema5a
Stxbp6
Nos1
Pax6
Pde11a
Cdh23
Kcns3
Cemip
Fbxl7
Gfra2
Reln
Lypd6
Otof
Meis2
Gm26871
Rnf220
Sema6d
Ecel1
Zeb2
Fign
Balap3
Piezo2
Zbtb7c
Percent Expressed
25 50 75 100
Average Expression
0.0 0.5 1.0 1.5 2.0

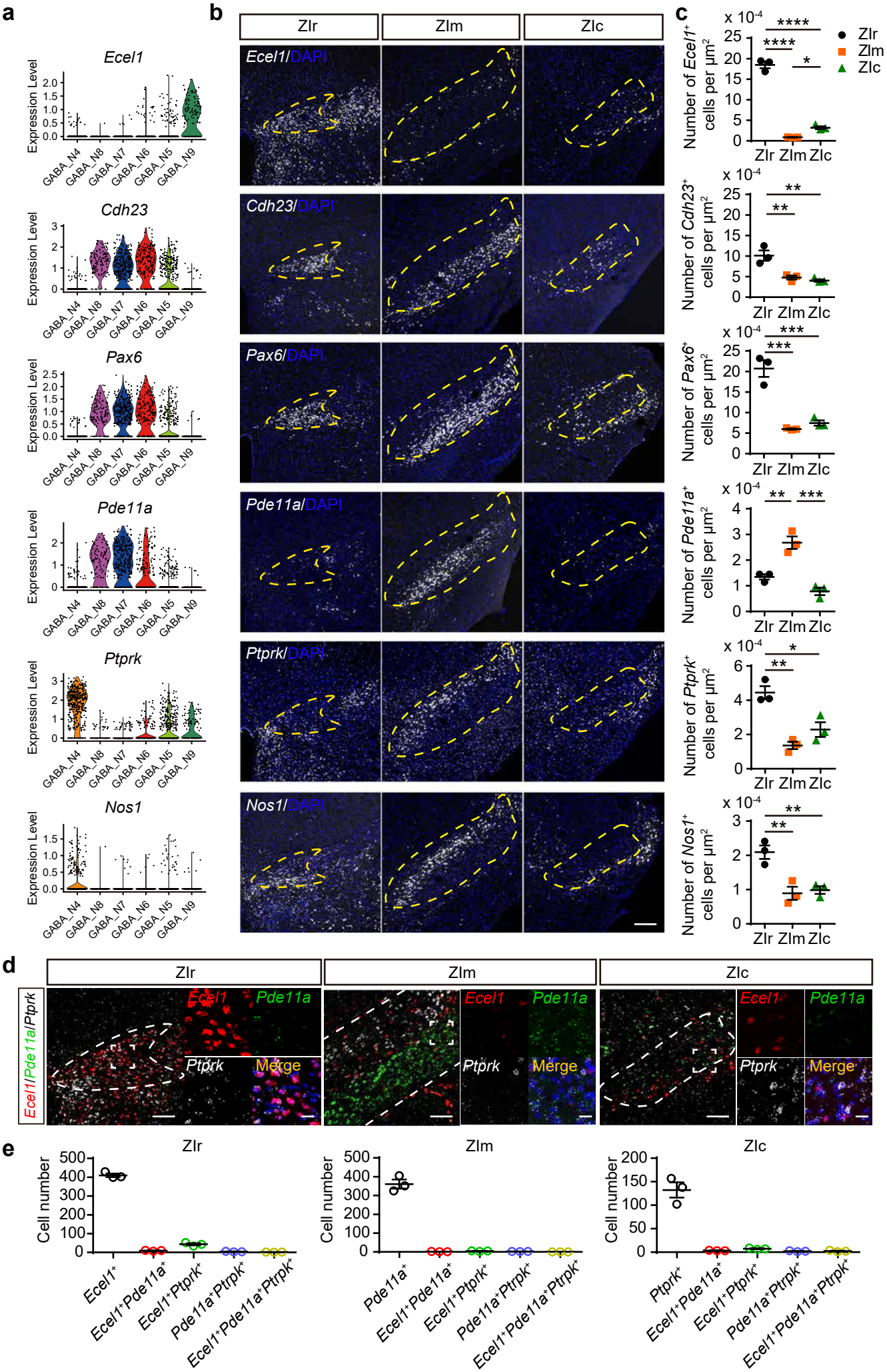
a
Ecel1
Cdh23
Pax6
Pde11a
Ptprk
Nos1
Expression Level
GABA_N4
GABA_N8
GABA_N7
GABA_N6
GABA_N5
GABA_N9
b
ZIr
ZIm
ZIc
Ecel1/DAPI
Cdh23/DAPI
Pax6/DAPI
Pde11a/DAPI
Ptprk/DAPI
Nos1/DAPI
c
Number of Ecel1+ cells per μm2
Number of Cdh23+ cells per μm2
Number of Pax6+ cells per μm2
Number of Pde11a+ cells per μm2
Number of Ptprk+ cells per μm2
Number of Nos1+ cells per μm2
x 10-4
d
Ecel1/Pde11a/Ptprk
Ecel1
Pde11a
Ptprk
Merge
e
Cell number
Ecel1+
Ecel1+Pde11a+
Ecel1+Ptprk+
Pde11a+Ptprk+
Ecel1+Pde11a+Ptprk+
Pde11a+
Ptprk+

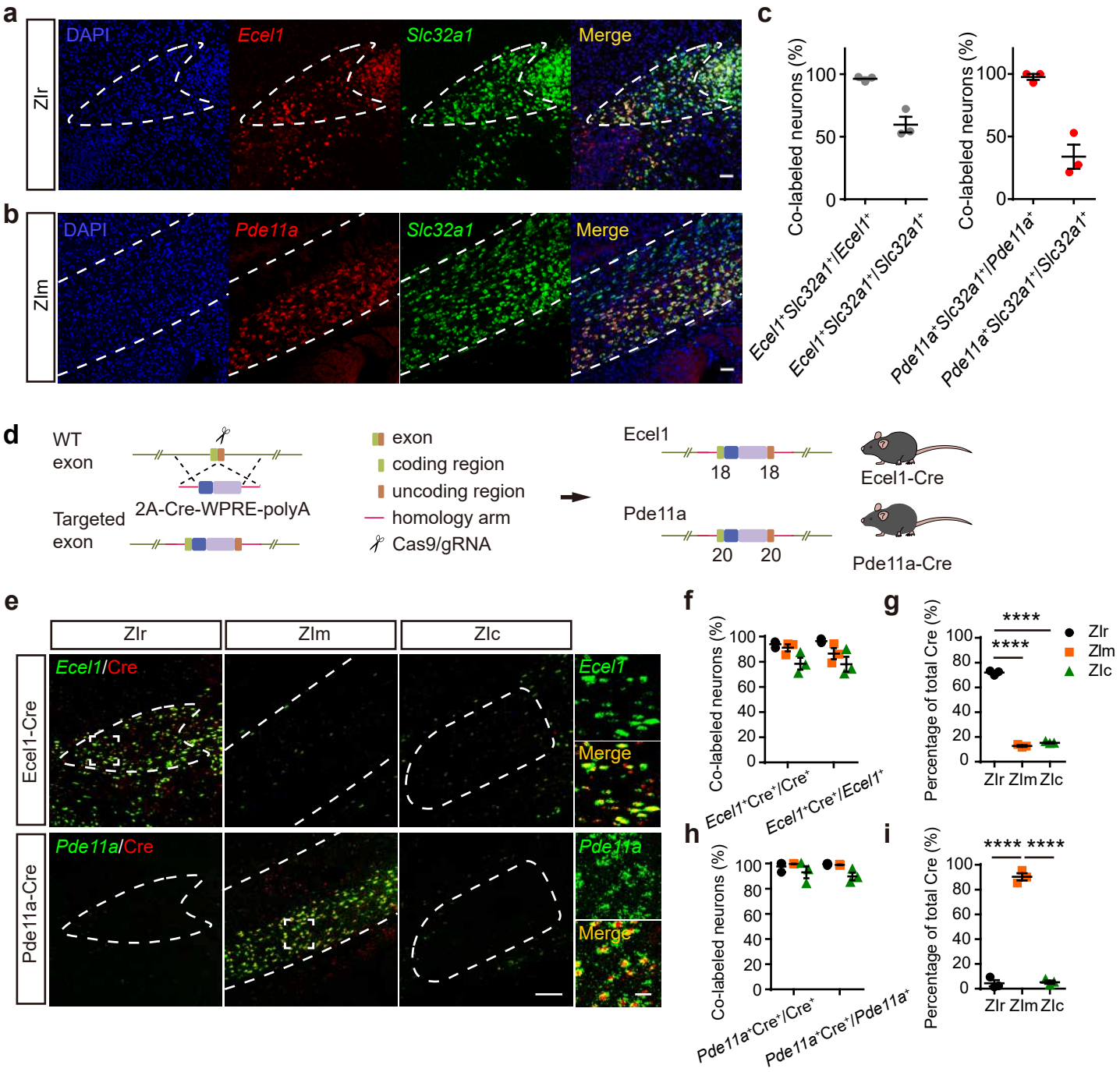
a
ZIr
DAPI
Ecel1
Slc32a1
Merge
b
ZIm
DAPI
Pde11a
Slc32a1
Merge
c
Co-labeled neurons (%)
100
50
0
Ecel1+Slc32a1+/Ecel1+
Ecel1+Slc32a1+/Slc32a1+
Pde11a+Slc32a1+/Pde11a+
Pde11a+Slc32a1+/Slc32a1+
d
WT exon
Targeted exon
2A-Cre-WPRE-polyA
exon
coding region
uncoding region
homology arm
Cas9/gRNA
Ecel1
18 18
Ecel1-Cre
Pde11a
20 20
Pde11a-Cre
e
ZIr
ZIm
ZIc
Ecel1-Cre
Ecel1/Cre
Ecel1
Merge
Pde11a-Cre
Pde11a/Cre
Pde11a
Merge
f
Co-labeled neurons (%)
100
80
60
40
20
0
Ecel1+Cre+/Cre+
Ecel1+Cre+/Ecel1+
g
Percentage of total Cre (%)
****
****
ZIr
ZIm
ZIc
ZIr ZIm ZIc
h
Co-labeled neurons (%)
Pde11a+Cre+/Cre+
Pde11a+Cre+/Pde11a+
i
Percentage of total Cre (%)
**** ****
ZIr ZIm ZIc

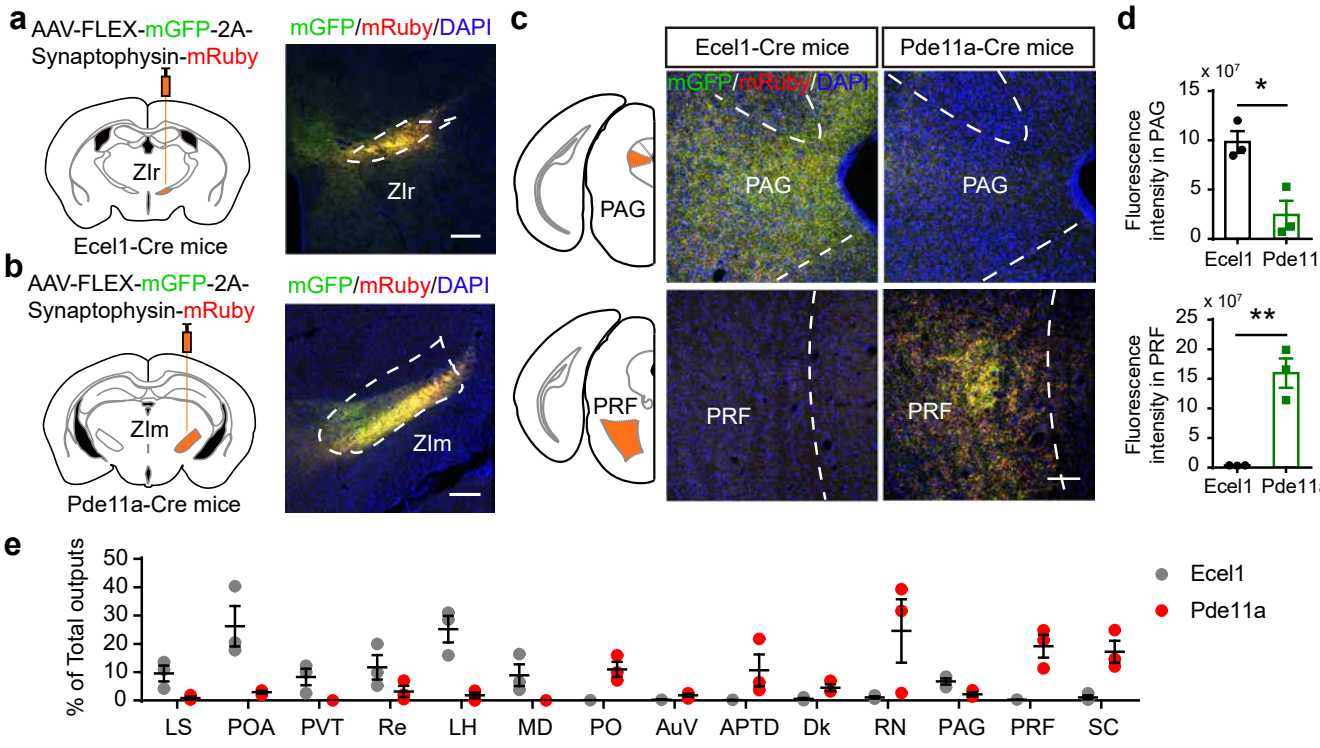
a
AAV-FLEX-mGFP-2A-Synaptophysin-mRuby
mGFP/mRuby/DAPI
ZIr
Ecel1-Cre mice
b
AAV-FLEX-mGFP-2A-Synaptophysin-mRuby
mGFP/mRuby/DAPI
ZIm
Pde11a-Cre mice
c
Ecel1-Cre mice
Pde11a-Cre mice
mGFP/mRuby/DAPI
PAG
PRF
d
Fluorescence intensity in PAG
x 10^7
Ecel1
Pde11a
Fluorescence intensity in PRF
e
% of Total outputs
Ecel1
Pde11a
LS
POA
PVT
Re
LH
MD
PO
AuV
APTD
Dk
RN
PAG
PRF
SC

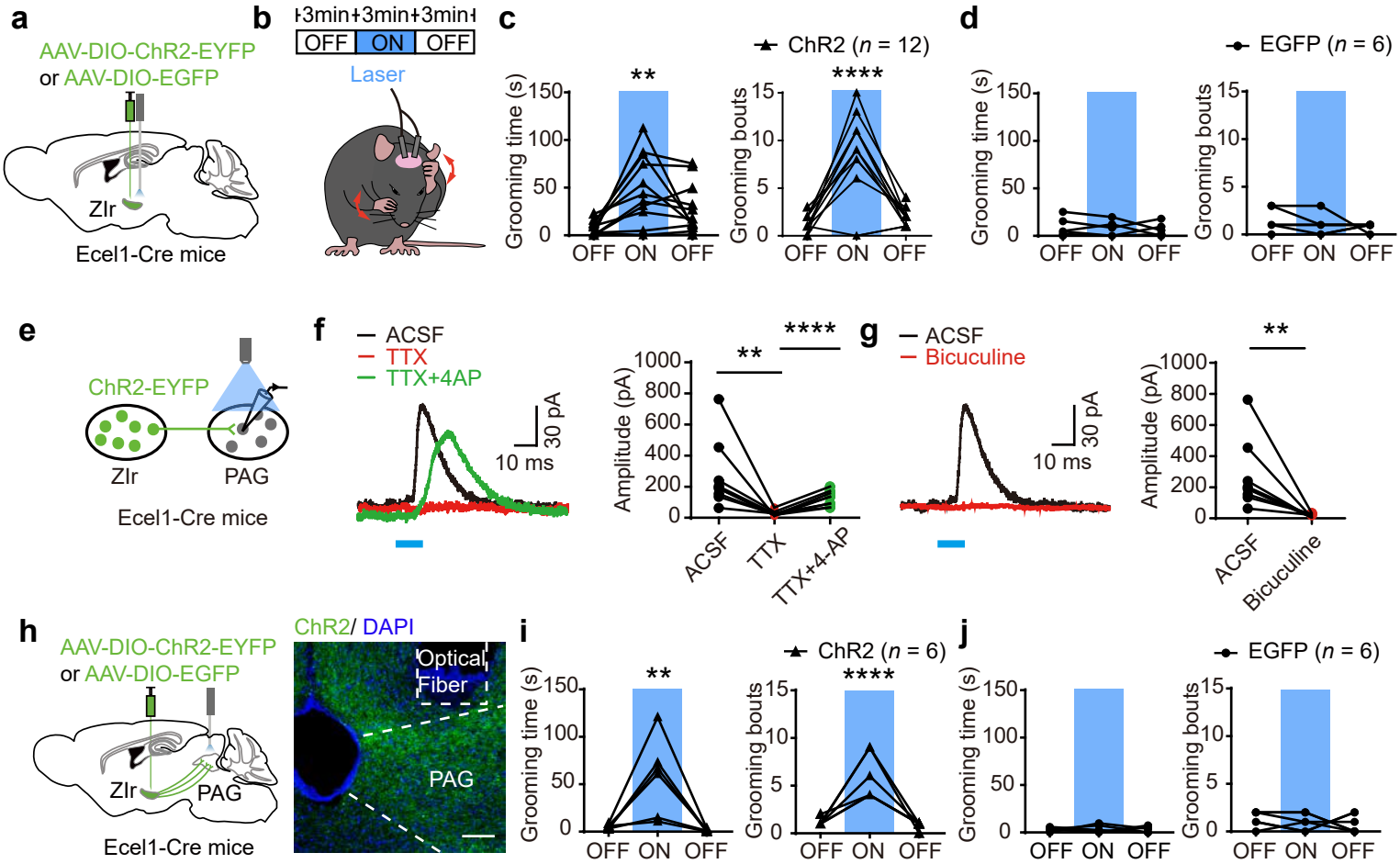
a
AAV-DIO-ChR2-EYFP
or AAV-DIO-EGFP
ZIr
Ecel1-Cre mice
b
3min
3min
3min
OFF
ON
OFF
Laser
c
ChR2 (n = 12)
Grooming time (s)
Grooming bouts
OFF ON OFF
d
EGFP (n = 6)
e
ChR2-EYFP
ZIr
PAG
Ecel1-Cre mice
f
ACSF
TTX
TTX+4AP
30 pA
10 ms
Amplitude (pA)
ACSF
TTX
TTX+4-AP
g
ACSF
Bicuculine
h
AAV-DIO-ChR2-EYFP
or AAV-DIO-EGFP
ZIr
PAG
Ecel1-Cre mice
ChR2/ DAPI
Optical Fiber
PAG
i
ChR2 (n = 6)
j
EGFP (n = 6)

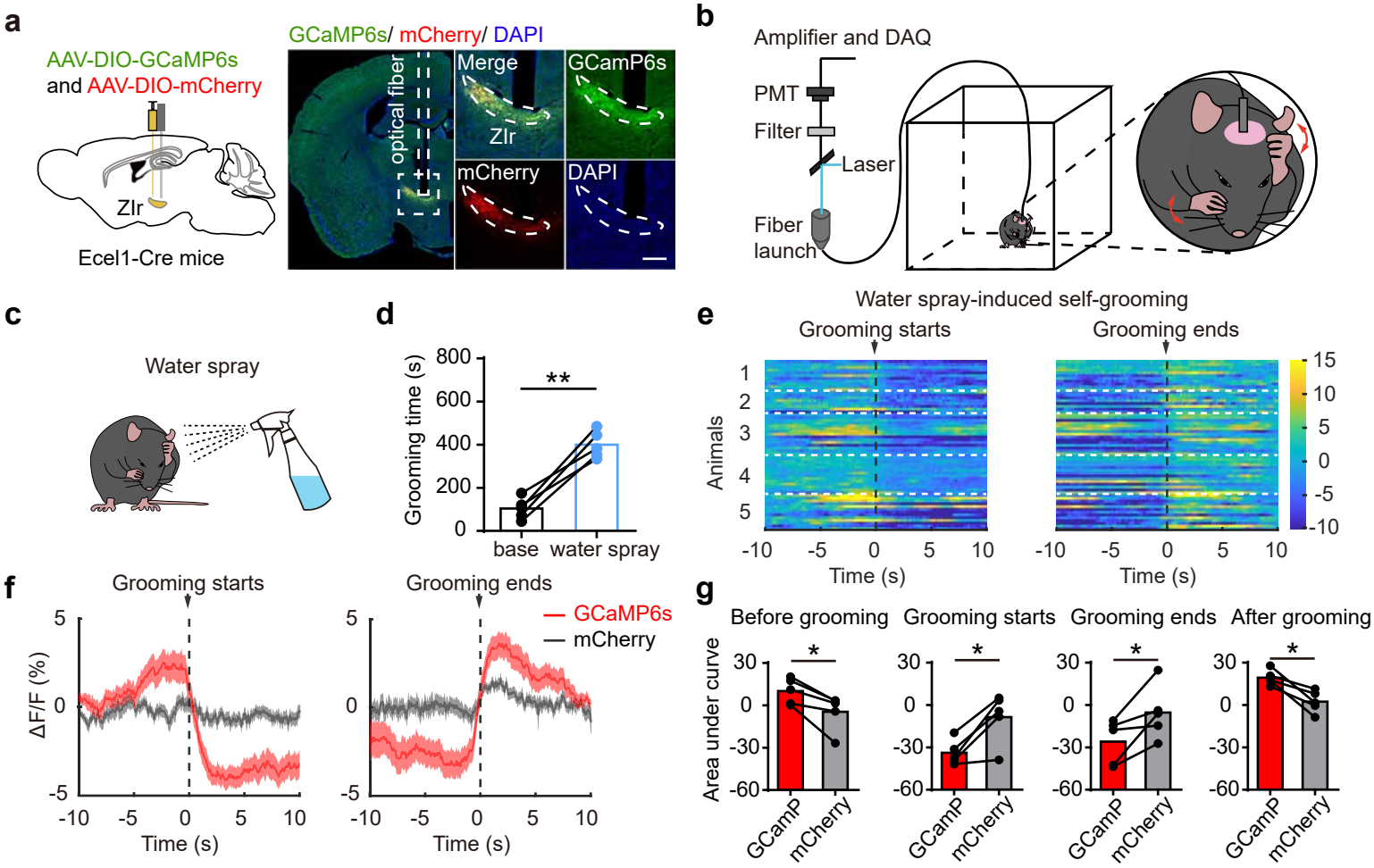
a
AAV-DIO-GCaMP6s
and AAV-DIO-mCherry
ZIr
Ecel1-Cre mice
GCaMP6s/ mCherry/ DAPI
optical fiber
Merge
ZIr
GCamP6s
mCherry
DAPI
b
Amplifier and DAQ
PMT
Filter
Laser
Fiber
launch
c
Water spray
d
Grooming time (s)
800
600
400
200
0
**
base
water spray
e
Water spray-induced self-grooming
Grooming starts
Grooming ends
Animals
1
2
3
4
5
-10
-5
0
5
10
Time (s)
15
10
5
0
-5
-10
f
Grooming starts
Grooming ends
ΔF/F (%)
5
0
-5
-10
-5
0
5
10
Time (s)
GCaMP6s
mCherry
g
Before grooming
Grooming starts
Grooming ends
After grooming
Area under curve
30
0
-30
-60
*
GCamP
mCherry

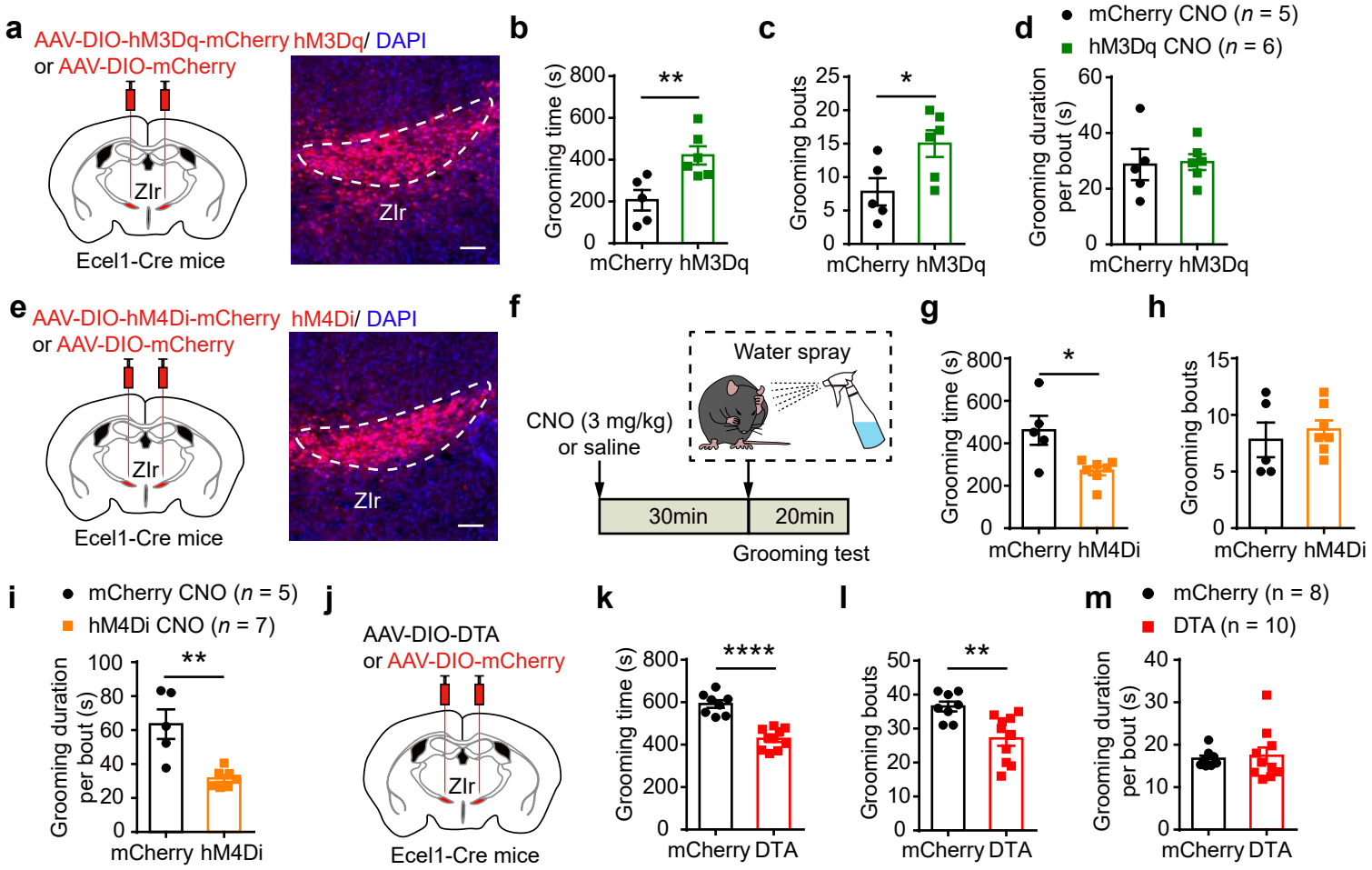
a
AAV-DIO-hM3Dq-mCherry
or AAV-DIO-mCherry
hM3Dq/ DAPI
ZIr
Ecel1-Cre mice
b
Grooming time (s)
mCherry hM3Dq
c
Grooming bouts
d
mCherry CNO (n = 5)
hM3Dq CNO (n = 6)
Grooming duration per bout (s)
e
AAV-DIO-hM4Di-mCherry
or AAV-DIO-mCherry
hM4Di/ DAPI
f
Water spray
CNO (3 mg/kg)
or saline
30min
20min
Grooming test
g
h
mCherry hM4Di
i
mCherry CNO (n = 5)
hM4Di CNO (n = 7)
j
AAV-DIO-DTA
or AAV-DIO-mCherry
k
mCherry DTA
l
m
mCherry (n = 8)
DTA (n = 10)

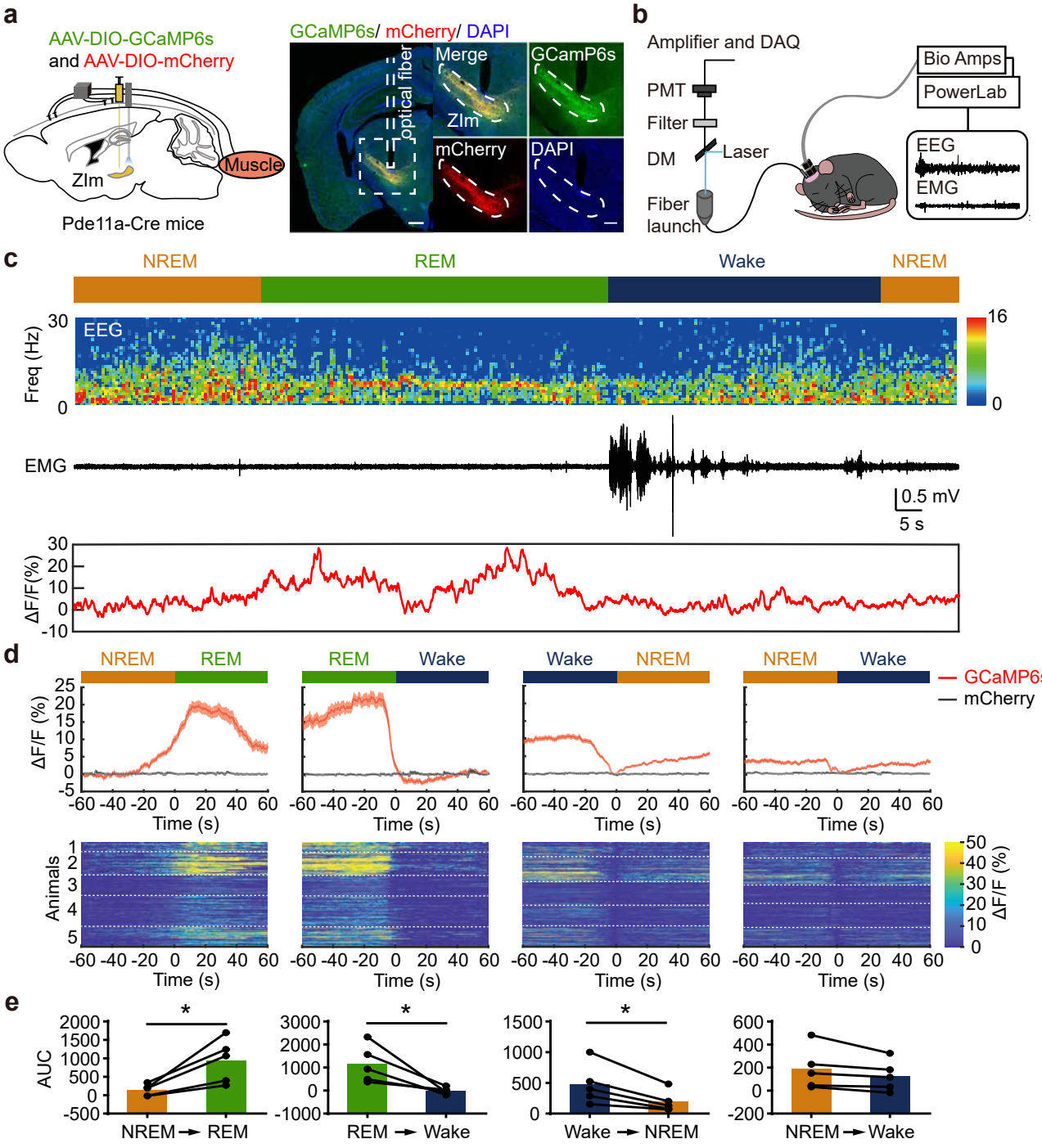
a
AAV-DIO-GCaMP6s
and AAV-DIO-mCherry
ZIm
Muscle
Pde11a-Cre mice
GCaMP6s/ mCherry/ DAPI
optical fiber
Merge
ZIm
GCamP6s
mCherry
DAPI
b
Amplifier and DAQ
PMT
Filter
DM
Laser
Fiber
launch
Bio Amps
PowerLab
EEG
EMG
c
NREM
REM
Wake
NREM
Freq (Hz)
EEG
EMG
0.5 mV
5 s
ΔF/F(%)
d
NREM
REM
REM
Wake
Wake
NREM
NREM
Wake
GCaMP6s
mCherry
ΔF/F (%)
Time (s)
Animals
ΔF/F (%)
e
AUC
NREM → REM
REM → Wake
Wake → NREM
NREM → Wake

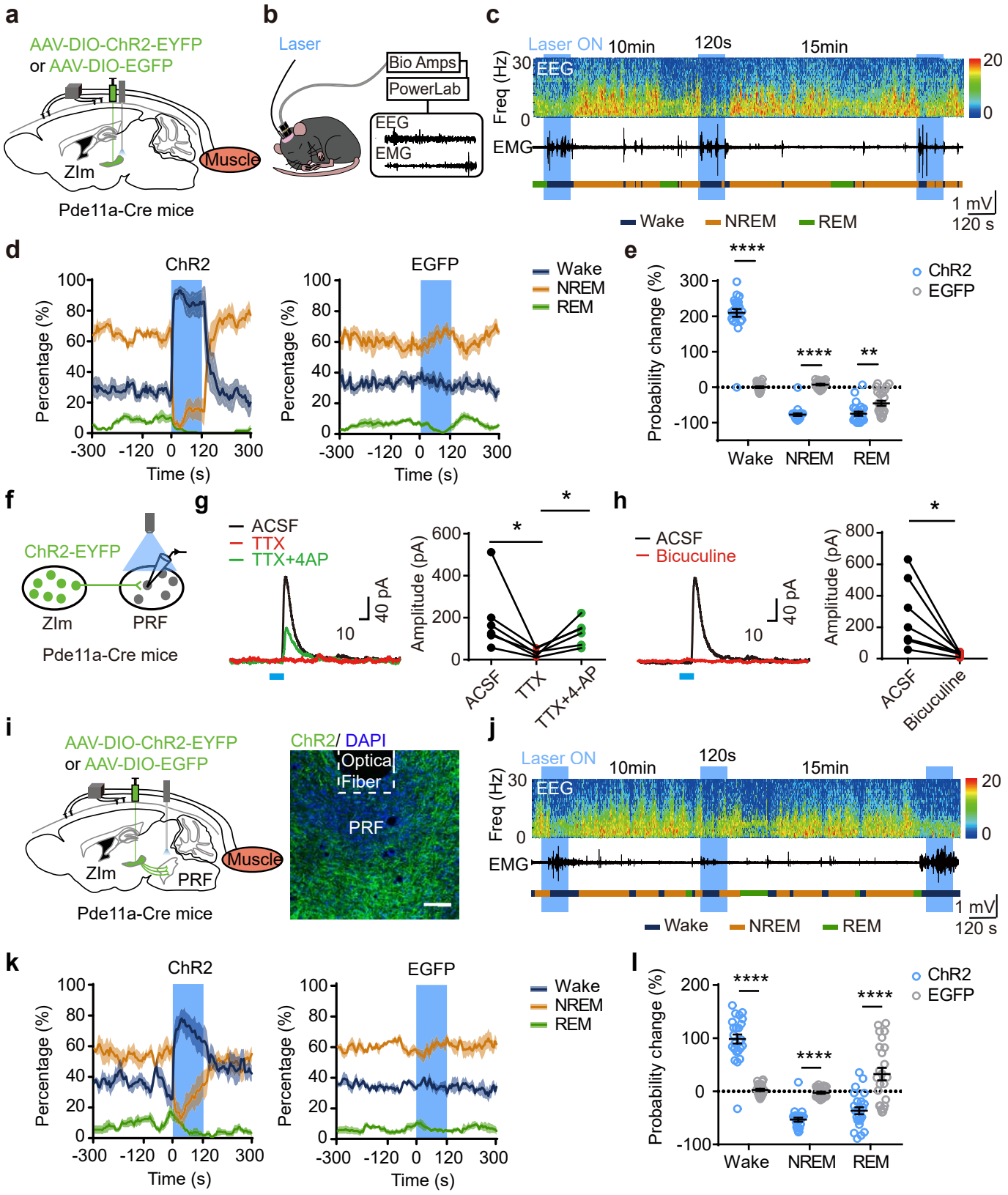
a
AAV-DIO-ChR2-EYFP
or AAV-DIO-EGFP
ZIm
Muscle
Pde11a-Cre mice
b
Laser
Bio Amps
PowerLab
EEG
EMG
c
Laser ON
10min
120s
15min
Freq (Hz)
30
0
EEG
EMG
20
0
1 mV
120 s
Wake
NREM
REM
d
ChR2
EGFP
Percentage (%)
Time (s)
Wake
NREM
REM
e
Probability change (%)
ChR2
EGFP
Wake
NREM
REM
f
ChR2-EYFP
ZIm
PRF
Pde11a-Cre mice
g
ACSF
TTX
TTX+4AP
40 pA
10
Amplitude (pA)
ACSF
TTX
TTX+4-AP
h
ACSF
Bicuculine
40 pA
10
Amplitude (pA)
ACSF
Bicuculine
i
AAV-DIO-ChR2-EYFP
or AAV-DIO-EGFP
ZIm
PRF
Muscle
Pde11a-Cre mice
ChR2/ DAPI
Optical
Fiber
PRF
j
Laser ON
10min
120s
15min
Freq (Hz)
30
0
EEG
EMG
20
0
1 mV
120 s
Wake
NREM
REM
k
ChR2
EGFP
Percentage (%)
Time (s)
Wake
NREM
REM
l
Probability change (%)
ChR2
EGFP
Wake
NREM
REM

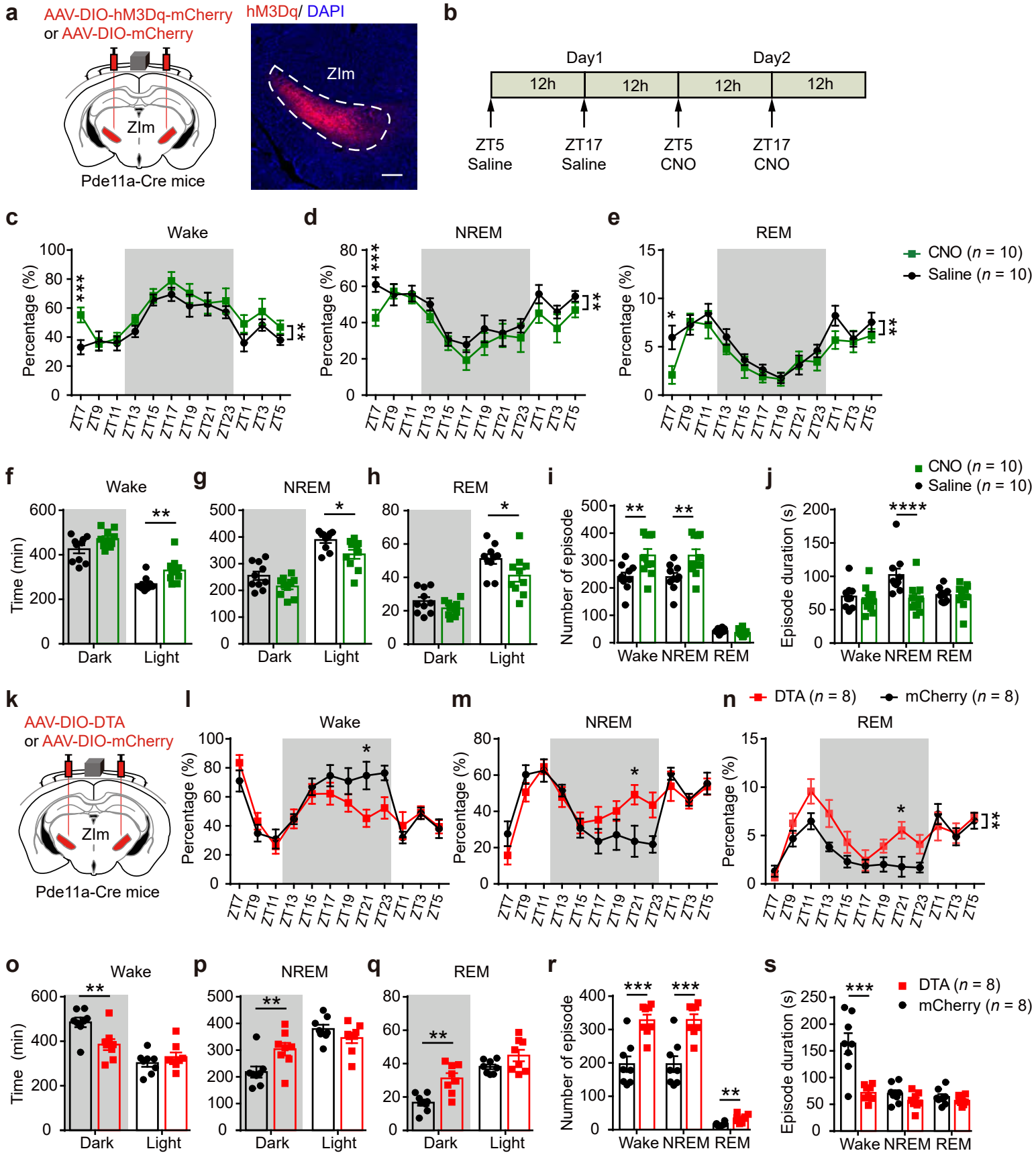
a
AAV-DIO-hM3Dq-mCherry
or AAV-DIO-mCherry
ZIm
Pde11a-Cre mice
hM3Dq/ DAPI
ZIm
b
Day1
Day2
12h
12h
12h
12h
ZT5
Saline
ZT17
Saline
ZT5
CNO
ZT17
CNO
c
Wake
Percentage (%)
d
NREM
e
REM
CNO (n = 10)
Saline (n = 10)
f
Wake
Time (min)
Dark
Light
g
NREM
h
REM
i
Number of episode
Wake NREM REM
j
Episode duration (s)
k
AAV-DIO-DTA
or AAV-DIO-mCherry
ZIm
Pde11a-Cre mice
l
Wake
m
NREM
n
REM
DTA (n = 8)
mCherry (n = 8)
o
Wake
p
NREM
q
REM
r
s